

Precession during merger 1: Strong polarization changes are observationally accessible features of strong-field gravity during binary black hole merger

R. O’Shaughnessy

*Center for Gravitation and Cosmology, University of Wisconsin-Milwaukee, Milwaukee, WI 53211, USA**

L. London, J. Healy, and D. Shoemaker

Center for Relativistic Astrophysics, Georgia Tech, Atlanta, GA 30332, USA

The short gravitational wave signal from the merger of compact binaries encodes a surprising amount of information about the strong-field dynamics of merger into frequencies accessible to ground-based interferometers. In this paper we describe a previously-unknown “precession” of the peak emission direction with time, both before and *after* the merger, about the total angular momentum direction. We demonstrate the gravitational wave polarization encodes the orientation of this direction to the line of sight. We argue the effects of polarization can be estimated *nonparametrically*, directly from the gravitational wave signal as seen along one line of sight, as a slowly-varying feature on top of a rapidly-varying carrier. After merger, our results can be interpreted as a coherent excitation of quasinormal modes of different angular orders, a superposition which naturally “precesses” and modulates the line-of-sight amplitude. Recent analytic calculations have arrived at a similar geometric interpretation. We suspect the line-of-sight polarization content will be a convenient observable with which to define new high-precision tests of general relativity using gravitational waves. Additionally, as the nonlinear merger process seeds the initial coherent perturbation, we speculate the *amplitude* of this effect provides a new probe of the strong-field dynamics during merger. To demonstrate the ubiquity of the effects we describe, we summarize the post-merger evolution of **104** generic precessing binary mergers. Finally, we provide estimates for the detectable impacts of precession on the waveforms from high-mass sources. These expressions may identify new precessing binary parameters whose waveforms are dissimilar from the existing sample.

I. INTRODUCTION

Coalescing comparable-mass black hole binaries are among the most likely and useful sources of gravitational waves for existing and planned gravitational wave detectors like LIGO [1], Virgo, [2], the Einstein telescope [3], and proposed space-based detectors. For sources in a suitable mass range, the signal these detectors receive contains significant features from the late-stage, strong-field dynamics of the black hole merger. Only full numerical simulations of Einstein’s equations can provide first-principles models for this epoch, including all dynamics and emission [4, 5]. Given the large computational cost per simulation, relatively few well-determined models have been produced.¹

For sufficiently high mass mergers, ground-based gravitational wave detectors are sensitive only to the short portion of the waveform provided by numerical simulations. Historical comparisons of the leading-order emission from comparable-mass nonprecessing binaries has suggested these waveforms look similar [5, 9]. Existing upper limits on gravitational waves from $> 50M_{\odot}$ merging binaries imply astrophysically plausible signal amplitudes for the first few detections must be low, at

best near the detection limit of the advanced LIGO and Virgo detectors [10]. Short, similar, low amplitude signals can carry a limited amount of information. Nonetheless, strong-field dynamics produce significant evolution in the emission beampattern and polarization content during merger. If in band, these features should be accessible to gravitational wave detectors.

In this paper we provide the first phenomenological description of the “kinematics of merger”. Rather than discuss properties of horizon or of the global spacetime [11, 12], we emphasize phenomenology of the asymptotic radiation. In particular, we identify precession-induced changes in the polarization content as an easily-accessible phenomenological measurable with which to distinguish between simulations. While we adopt a simple model to characterize this diagnostic, our results can be translated to fully-developed parameter estimation and model selection strategies, which fit data to a model using physically-motivated [13–18] and phenomenological [19–21] signal parameters. For clarity we use three examples to illustrate the precession we have in mind and the imprint it makes on emitted signals. To demonstrate the features we describe occur frequently and to connect those features to quasinormal mode frequencies, we also describe the post-merger dynamics of a much larger array of simulations. In Section II we describe the gravitational wave signals, preferred orientations, and description of polarization we use in our work. We argue our practical approach to gravitational wave polarization, decomposing the line of sight signal into left- and right-handed components, is both observationally accessible and intuitive.

*Electronic address: oshaughn@gravity.phys.uwm.edu

¹ Most simulations have thoroughly explored nonspinning and spin-aligned binaries [5]. Some simulations with more generic spin have been performed (e.g., to study gravitational wave recoil kicks) [6–8].

Our study uses detailed numerical relativity simulations of the late inspiral and merger of two binary black holes, in general both with spin. By example, we demonstrate that “precession” dynamics, suitably defined, continues after merger. Again using selected examples, we illustrate that *each line of sight* encodes the relative orientation of the (time dependent, precessing) preferred orientation. By comparing these to a simple expression, we argue this behavior occurs in general, for all lines of sight and all precessing binaries. In Section III we demonstrate that all these features change significantly, depending on the spin magnitudes and orientations adopted. Based on these investigations, we anticipate the polarization content can trace features of the strong-field merger event. Then, in Section IV, we demonstrate that this polarization information is experimentally accessible: similar waveforms differing primarily through their polarization content (i.e., time history of left- versus right-handed) can be observationally distinguished. We demonstrate observations can weakly constrain orientation evolution *nonparametrically*, independent of other information naturally encoded in the gravitational wave signal.

A. Context

Though the gravitational-wave signal from merging binaries nominally encodes all information about the space-time, previous investigations of the (2, 2) mode suggest universality of the merger signal [5, 9], providing the informal impression that previously hypothesized complicated nonlinearities in general relativity do not significantly complicate the short signal from the merger epoch. In other words, simulations suggest the merger signal provides little unambiguous information about strong-field general relativity. However, the unique contribution of merger to the waveforms is invariably mixed with the preceding (inspiral) and subsequent (ringdown) signal, making nonlinear behavior difficult to identify. In principle the mass loss, angular momentum change, and recoil kick can all be tabulated, fit, and constrain the nonlinear response at merger. Nevertheless, in practice the contribution from merger cannot be cleanly distinguished from the contributions from inspiral and ringdown. While symmetry demands a general form [22], symmetry does not strongly forbid inspiral or merger epochs from contributing to these integrated quantities. The contribution from merger can be partially disentangled in the time domain, plotting fluxes like dE/dt , or possibly the time-angular domain. Unfortunately, investigations looking for strong mode-mode couplings indicative of nonlinearity have recovered the familiar perturbative results [23–25]. Previous investigations suggest that the asymptotic radiation encodes preferred directions with *different* symmetry properties, not tied to the orientations associated with standard conserved constants. These orientations are well resolved through merger and seem to evolve non-trivially both before and after the merger [26, 27]. This

preferred orientation may therefore provide a new signature of strong-field dynamics.

After this study was completed, we became aware of an analytic study providing a simple, geometric interpretation of (short-wavelength) quasinormal modes’ frequencies as precession [28]. Their calculation extended previous estimates derived in the slow-rotation limit to arbitrary spin. We find a similar result at the lowest multipolar order, even in the strong field: all modes precess at a nearly constant rate during and after merger.

II. SIMULATIONS AND DIAGNOSTICS

A. Simulations I: Overview

The simulations examined in this paper will be described at greater length in a companion publication. Physically, these binary configurations correspond to an unequal-mass generalization of the “S series” [6], where one spin is in the orbital plane $\mathbf{a}_1 = a\hat{x}$ and the other spin rotates through the (x, z) plane with comparable dimensionless spin $a = |\mathbf{S}/M^2|$. Initial data was evolved with *Maya*, which was used in previous binary black hole (BBH) studies [6–8, 29–33]. The grid structure for each run consisted of 10 levels of refinement provided by *CARPET* [34], a mesh refinement package for *CACTUS* [35]. Sixth-order spatial finite differencing was used with the BSSN equations implemented with *Kranc* [36]. Initial binary properties and simulation details including initial separation, spin configuration, and finest resolution are detailed in Table I. In the text, we present results for the fiducial simulation at $r = 90M$ unless otherwise indicated. The choice of extraction radius has minimal impact on the results shown here.

To consistently illustrate features of these simulations, we will emphasize one fiducial binary, denoted Sq(4,0.6,90,9) with $m_1/m_2 = 4$, $a_1 = 0.6\hat{x} = -a_2$, placed in orbit in the x, y plane with a coordinate separation $d = 9M$; see Table I for details.² Figure 1 shows the corresponding inspiral-merger trajectories of the orbital angular momentum and spin directions, $\hat{L}(t)$ and $\hat{S}_1(t)$, where $\hat{S}_1(t)$ corresponds to the larger black hole. Initially, the binary’s orbital angular momentum is larger but comparable to $\mathbf{S}_1 = \mathbf{a}_1 m_1^2$; both are much larger than the companion’s spin. Early in the inspiral, $\hat{L}(t)$ and $\hat{S}_1(t)$ precess around the total angular momentum direction [37]. During this process, the three angular momenta (J, L and S_1) are nearly coplanar, with the angle between L and \vec{S}_1 roughly constant, as expected from the post-Newtonian limit. By contrast, as the orbit transitions from inspiral to plunge, the (coordinate) orbital angular

² Our fiducial initial conditions are comparable to those adopted in a companion paper on orientation-dependent emission [27].

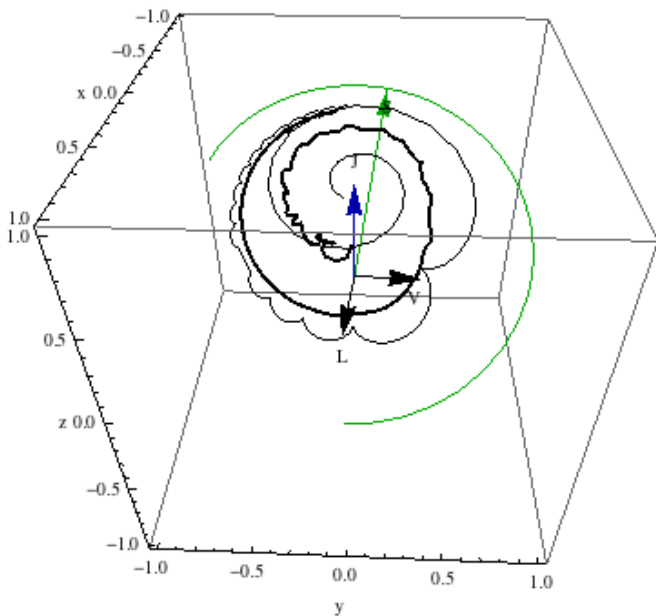


FIG. 1: **Evolution of angular momenta and \hat{V} with time:** For one simulation (Tq(4,0.6,90), with $m_1/m_2 = 4$, $a_1 = 0.6\hat{x}$, $a_2 = 0.6\hat{z}$ starting at $d = 10M$), a plot of the preferred direction \hat{V} (thick black; see Eq. (1)) superimposed on the coordinate orbital (black) and spin (green) angular momenta directions \hat{L}, \hat{S}_1 as a function of time. The paths indicate how all three evolve with time; the arrows are evaluated at a specific instant shortly before merger. A blue arrow also indicates the final (\simeq initial) total angular momentum \hat{J} . At very early times, the directions \hat{V} and \hat{L} nearly agree [38]; at merger, however, \hat{L} converges to \hat{J} while \hat{V} continues to precess. Compare to figures in O’Shaughnessy et al. [27].

momentum *converges* towards the total angular momentum direction. The spin direction, by contrast, changes far less dramatically during the plunge and merger.

B. Preferred orientations

Conserved quantities of the spacetime and radiation escaping to infinity encode several preferred orientations. One preferred, manifestly physical, but nearly-time-independent orientation is \hat{J} , the nearly conserved orientation of the total angular momentum. Another orientation extremizes the quadrupolar radiation, such that the (2, 2) mode of the Weyl scalar is largest [39, 40]; we denote this orientation as $\hat{Q}(t)$. Finally, a third orientation $\hat{V}(t)$ is the principal axis of [26, 27, 38]

$$\begin{aligned} \langle \mathcal{L}_a \mathcal{L}_b \rangle &\equiv \frac{\int d\Omega \psi_4^*(t) \mathcal{L}_a \mathcal{L}_b \psi_4(t)}{\int d\Omega |\psi_4|^2} \\ &= \frac{\sum_{lm} \psi_{4lm}^* \psi_{4lm} \langle lm' | \mathcal{L}_a \mathcal{L}_b | lm \rangle}{\int d\Omega |\psi_4|^2} \end{aligned} \quad (1)$$

where \mathcal{L} are rotation group generators; where ψ_4 is the Weyl scalar; and where in the second line we expand

$\psi_4 = \sum_{lm} \psi_{4lm}(t) Y_{lm}^{(-2)}(\theta, \phi)$ and perform the angular integral; see Ochsner and O’Shaughnessy [38] for explicit formulae.

These three quantities do not agree. For example, early in the inspiral \hat{J} is manifestly distinct from the two precessing, dynamic orientations \hat{V}, \hat{Q} , which both nearly correspond to \hat{L} [38, 39]. The two dynamic orientations also generally differ, albeit less significantly.³ As a concrete example, if the Weyl scalar consists only of the $l = 2$ subspace with the time-independent value

$$\psi_{42m} = Y_{22}^{(-2)} + Y_{2,-2}^{(-2)} + (Y_{2,1}^{(-2)} + Y_{2,-1}^{(-2)})/4 + Y_{20}^{(-2)}/2(2)$$

then on the one hand our preferred direction has $\hat{V} \simeq \hat{n}(0.05, 0)$ but the direction that maximizes the (2, 2) mode lies along $\hat{n}(0.25, 0)$, where $\hat{n}(\theta, \phi)$ is a cartesian unit vector with polar coordinates θ, ϕ . For simplicity, in this work we only present results for a single dynamic orientation \hat{V} .

Figure 1 shows the trajectories of \hat{L}, \hat{V} and \hat{J} . While \hat{L} and \hat{V} nearly agree prior to merger, they differ significantly at and after merger. In the time domain, the direction \hat{V} roughly corresponds to the direction of peak $|\psi_4|$. More critically, when averaged over mass and frequency, this direction corresponds very closely to the direction of largest signal amplitude

$$\rho^2 \equiv 2 \int_{-\infty}^{\infty} \frac{df}{S_h} \frac{|\psi_4(f, \hat{n})|^2}{(2\pi f)^4} \quad (3)$$

where we adopt the isotropic two-detector network definition of ρ^2 used in O’Shaughnessy et al. [27]. Moving forward in time, both \hat{V} and \hat{L} precess around the total angular momentum \hat{J} [37]. When the two black holes merge, the orbital angular momentum has converged to the total angular momentum ($\hat{L} \rightarrow \hat{J}$). This direction no longer evolves past merger. By contrast, the observationally-relevant direction \hat{V} continues to evolve through and beyond merger.

As will be demonstrated using the fiducial simulation, different preferred directions identify different physics. In particular, \hat{V} is directly connected to observations, and indicates interesting new dynamics that could be imprinted on the gravitational wave signal.

Here, we identified this imprint at each time using *all gravitational wave emission directions*. Experiments have access to only one line of sight. Below, we describe a concrete method to identify the imprint of \hat{V} using only a single emission direction, via the polarization evolution versus time.

³ While the differences between the two approaches to preferred orientations are often small in *absolute* scale, these small angular differences imply significant disagreement about the relative magnitude of strongly suppressed modes, particularly in the merger phase.

C. Line of sight diagnostics: amplitude, phase, polarization

Real gravitational wave detectors only have access to a single line of sight. Despite this limitation, they still have access to the rich and distinctive modulations that the orbit and precession imparts on the line-of-sight time-evolving gravitational wave signal, $h \equiv h_+ + ih_\times$. To interpret these modulations, we change basis from the standard linear polarizations (h_+, h_\times) to two circular polarizations (h_R, h_L with $h = h_R + h_L$). Strictly, we split the Weyl scalar ψ_4 rather than $h(t)$, to minimize errors from poorly-constrained early-time and late-time effects.⁴ We will see below that precession distinctively modulates the amplitude and phase of both circular polarizations.

The left and right-handed circularly polarized parts of $\psi_4(t)$ are naturally isolated in the frequency domain [27]: positive frequency components are right-handed, and negative frequency components are left-handed. In the time domain, this procedure corresponds to convolution of h with a specific (acausal) kernel:

$$\psi_{4R} = \int_0^\infty df \tilde{\psi}_4(f) e^{-2\pi i f t} \quad (4a)$$

$$= \int_{-\infty}^\infty d\tau K_R(t - \tau) \psi_4(\tau) \quad (4b)$$

$$K_R(\tau) = \lim_{\epsilon \rightarrow 0^+} \frac{-i}{\tau - i\epsilon} \frac{1}{2\pi} \quad (4c)$$

$$\psi_{4L} = \int_{-\infty}^0 df \tilde{\psi}_4(f) e^{-2\pi i f t} \quad (4d)$$

$$K_L(\tau) = \lim_{\epsilon \rightarrow 0^+} \frac{+i}{\tau + i\epsilon} \frac{1}{2\pi} \quad (4e)$$

where $K_{R,L}(\tau)$ are suitable inverse fourier transforms of the unit step function. For each polarization, we can define an amplitude $|h_R|$ and phase $\arg(h_R)$. In general, the amplitude evolves on a precession (or, if none, radiation reaction) timescale; the phase increases secularly, on a radiation reaction timescale, with precession-induced modulations on shorter timescales [37].

This procedure for separating left- and right-handed signals can be performed with real gravitational wave data. For each line of sight, experiments with comparable sensitivity to two linear polarizations can reorganize their data analysis procedure to be sensitive to only these left- or right-handed polarizations. Additionally, this projection process has physically expected properties, applied

to nonprecessing binaries. The angular modes ψ_{4lm} describe emission preferentially above ($m > 0$) or below ($m < 0$) the orbital plane, where m is the mode order (i.e., each term in $\psi_4 = \sum_{lm} \psi_{4lm} Y_{lm}^{(-2)}(\theta, \phi)$'s mode decomposition is proportional to some $\psi_{4lm} \exp(im\phi)$). One can empirically verify that the angular modes from nonprecessing binaries are nearly chiral:

$$\tilde{\psi}_{4lm}(f) \simeq 0 \quad \text{for } mf < 0 \quad (5)$$

In the stationary-phase limit, this relationship corresponds to a desirable and usually satisfied requirement on the angular frequency versus time:⁵ $\partial_t \arg \psi_{4lm}$ is monotonically increasing for $m > 0$ and decreasing for $m < 0$. For nonprecessing binaries, to a good approximation our polarization projection corresponds to eliminating modes of either $m < 0$ (projecting to R) or $m > 0$ (projecting to L).

To decouple polarization content from secular trends in amplitude and phase seen in nonprecessing binaries, we once again change variables from $\psi_{4R,L}$ (2 complex or 4 real quantities) to a real typical amplitude A , a real typical phase Φ , and a complex polarization amplitude z (one complex and two real quantities):

$$z \equiv \frac{\psi_{4L}^*}{\psi_{4R}} \quad (6)$$

$$A^2 \equiv |\psi_{4L}|^2 + |\psi_{4R}|^2 \quad (7)$$

$$e^{i\Phi} \equiv \left(\frac{\psi_{4L}^* \psi_{4R}}{\psi_{4L} \psi_{4R}^*} \right)^{1/2} \quad (8)$$

By construction, the polarization amplitude z is nearly constant for nonprecessing binaries whose gravitational wave emission is dominated by equal in magnitude and conjugate in phase (l, m) = (2, 2) and (2, -2) modes. In this limit, the Weyl scalar asymptotically takes the form

$$r\psi_4(\hat{n}, t) = \frac{A(t)}{\sqrt{2}} [e^{i\Phi(t)} Y_{22}^{(-2)}(\hat{n}) + e^{-i\Phi(t)} Y_{2,-2}^{(-2)}(\hat{n})] \quad (9)$$

To recover the correct limits along the \hat{z} axis (i.e., the $\pm \hat{z}$ direction), the basis coefficients of the two spin-weighted harmonics $Y_{2\pm 2}^{(-2)}$ are necessarily right and left circularly polarized. As a result, for a signal dominated by equal and conjugate (2, 2) and (2, -2) modes, the polarization amplitude is a time-independent and purely geometrical expression:

$$z_\psi \simeq Y_{2,-2}^{(-2)*}(\hat{n}) / Y_{2,2}^{(-2)}(\hat{n}) = e^{i4\Psi_L} \frac{(1 - \cos\theta)^2}{(1 + \cos\theta)^2} \quad (10)$$

where $\theta = \cos^{-1} \hat{L} \cdot \hat{n}$ and Ψ_L characterize the orientation of the orbital angular momentum along the line of sight and in the plane of the sky, respectively; see, e.g. [41].

⁴ We anticipate the gravitational wave content of the (2, 2) mode to be almost exclusively right-handed. However, the linear transformation from $h \rightarrow h_{R,L}$ is highly nonlocal, depending in principle on arbitrarily early and late times. The gravitational wave strain at the start (inspiral) or end (nonlinear memory) can be significant. By contrast, the Weyl scalar's diminished early-time amplitude and lack of memory terms leads to a well-behaved projection.

⁵ Due to projection effects of spheroidal harmonics onto spherical harmonics, this property need not hold for all higher-order modes. We will not address angular mode mixing in this paper.

Reversing the sense of the approximation above, assuming instantaneous and symmetric $(2, \pm 2)$ emission along a proposed slowly-varying orientation $\hat{O}(t)$, we estimate the polarization content $\hat{z}_O(t)$ along a line of sight \hat{n} by

$$\begin{aligned}\hat{z}_O &= \frac{[\hat{O} \cdot (\hat{x}_n + i\hat{y}_n)]^4 (1 - \hat{O} \cdot \hat{n})^2}{(1 - (\hat{O} \cdot \hat{n})^2)^2 (1 + \hat{O} \cdot \hat{n})^2} \\ &= \frac{[\hat{O} \cdot (\hat{x}_n + i\hat{y}_n)]^4}{(1 + \hat{O} \cdot \hat{n})^4}\end{aligned}\quad (11)$$

where the two vectors \hat{x}_n, \hat{y}_n define a frame of reference in the plane of the sky, perpendicular to \hat{n} . As this simple approximation suggests, for a precessing binary the polarization amplitude \hat{z}_ψ should fluctuate, reflecting the relative importance and phasing of left- and right-handed emission in the instantaneous signal.

Closer to the orbital plane, the balance of polarizations is nearly equal ($|z| \simeq 1$). This naturally finely-tuned region involves near-perfect cancellation of (some of) the leading-order emission,⁶ allowing higher-order angular dependence to contribute significantly to the polarization content. Unlike the leading-order factors, these higher-order multipoles sometimes treat the component masses *asymmetrically*. As a result, the waveform and polarization content near the orbital plane has additional modulations at the orbital period. For example, for a nonprecessing binary with both conjugate and symmetric emission in all modes, the Weyl scalar has the form

$$r\psi_4(\hat{n}, t) = \sum_{m=1}^2 a_m(t) [e^{i\Phi_m(t)} Y_{2m}^{(-2)}(\hat{n}) + e^{-i\Phi_m(t)} Y_{2,-m}^{(-2)}(\hat{n})] \quad (12)$$

As instantaneous quadrupole emission almost always dominates, the polarization amplitude z can be approximated by an oscillating but nearly-constant correction to the leading order term [Eq. (10)]:

$$z_\psi \simeq e^{i4\psi_L} \left(1 + \frac{4a_2 e^{-i(\phi - \Phi_1 + \Phi_2)} \cot \theta}{a_1} + \dots \right) \quad (13)$$

In short, for orientations where higher harmonics contribute significantly, the polarization amplitude z_ψ should oscillate, with the peak-to-trough amplitude in one-to-one relation to the magnitude of these harmonics.

To summarize, any gravitational wave signal can be decomposed into two polarizations $\psi_{4R,L}$. Using the complex amplitude $z = \psi_{4L}^* / \psi_{4R}$ to characterize the relative proportion and phasing of each signal, we find that polarization content encodes information about the merging binary on at least two scales. On the one hand, on long

precession timescales, the polarization amplitude tells us how the preferred emission direction evolves; see, e.g., Eq. (11). On these scales, the complex amplitude can vary significantly. On the other hand, on the orbital and eventually merger timescale, rapid small oscillations in the polarization amplitude directly measure the relative proportion of $(2, \pm 1)$ modes. These modes are produced naturally in asymmetric or eccentric binaries along certain lines of sight. Finally, in our analysis we have for simplicity assumed symmetric emission in the $(2, \pm 2)$ modes. However, when expressed in a corotating frame [26], many of our simulations emit asymmetrically, with one mode preferentially larger than another during the merger and ringdown phase. Without foreknowledge of this bias, the simple estimates used above would, if inverted, recover the incorrect inclination of the preferred emission direction relative to the line of sight. In other words, while the complex polarization amplitude z manifestly encodes information about the preferred orientation's evolution relative to the line of sight and about the relative significance of higher modes, we cannot unambiguously interpret this information unassisted by a large catalog of candidate waveforms. For the purposes of this paper, we will treat $z(t)$ itself as a phenomenological observable.

D. Line of sight diagnostics: Three examples

To illustrate the power of this decomposition, Figures 2, 3 and 4 apply it to a nonprecessing and precessing $q = 4$ binary, respectively.

Figure 2 demonstrates our polarization decomposition with a nonprecessing $q = 4$ binary, extracting the Weyl scalar along a “generic” direction $[(\theta, \phi) = (60^\circ, 205^\circ)]$. For a nonprecessing binary, the gravitational wave signal is dominated by quadrupole emission from the $(2, \pm 2)$ modes. To an excellent approximation, the two polarizations $\psi_{4R,L}$ (red and blue curves in this figure) are proportional to one or the other of these modes, respectively, with the proportionality constants set geometrically by spin-weighted harmonics [Eq. (9)] and hence the inclination. However, this line of sight is close enough to the orbital plane that the $(2, \pm 1)$ mode can contribute significantly. As demonstrated with the dotted line in the bottom panel of Figure 2, these modes beat against the leading-order quadrupole, causing the complex polarization z to oscillate by roughly ten percent during the inspiral at roughly the orbital period. Higher-order angular modes $l > 2$ also beat against the leading-order quadrupole. Including these terms in the the sum $\sum_{lm} \psi_{4lm} Y_{lm}^{(-2)}$ produces richer time dependence along each line of sight, in both polarizations (solid curves in the top panel of Figure 2). Nonetheless, the ratio of the two polarizations (z) still behaves like the $l = 2$ result.

Precessing binaries, by contrast, generally exhibit dramatic changes in polarization. Figure 3 shows features of the precessing $m_1/m_2 \equiv q = 4$ binary started with

⁶ Near the orbital plane of a nonprecessing binary, gravitational wave emission is nearly linearly polarized.

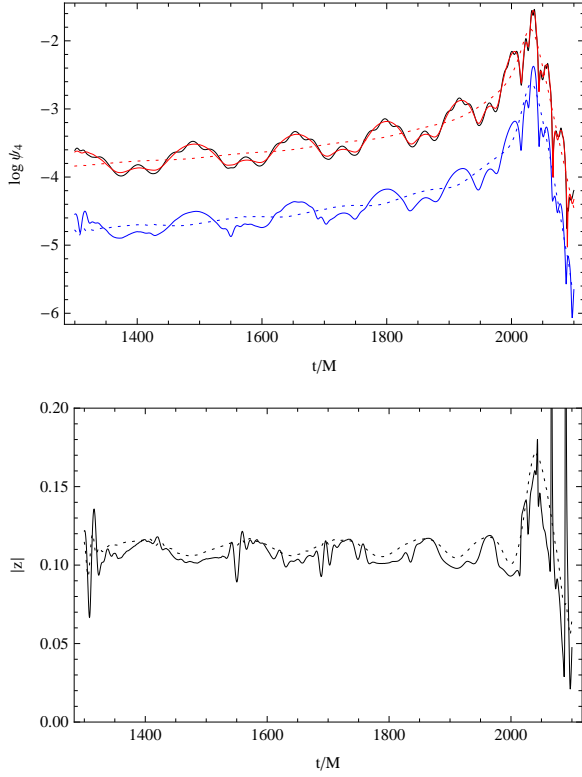


FIG. 2: Polarization imprints on signal 1: Nonprecessing: For a nonspinning $q = 4$ binary, two measures of the polarization content along $(\theta, \phi) = (60^\circ, 205^\circ)$. Results are shown including all angular modes ψ_{4lm} with $l \leq 4$ (solid) and just retaining terms with $l = 2$ (dotted). *Top panel:* The line of sight right and left-handed amplitudes $|\psi_{4R,L}|$ (red R, blue L). For this and almost all other lines of sight, a single helicity dominates for all time. For comparison, the solid black line shows $|\psi_4| = |\psi_{4R} + \psi_{4L}|$. *Bottom panel:* $\text{Re} z_\psi = \text{Re} \psi_{4L}^* / \psi_{4R}$ versus time. Though one helicity dominates, the polarization content oscillates significantly at the orbital period. These oscillations are proportional to the “higher-mode” content ($2, \pm 1$) and therefore measure the mass ratio or residual eccentricity.

$\vec{a}_1 = 0.6\hat{x} = -a_2$ at a coordinate separation $d = 9M$, as used in [27]. As seen in the top panel, the balance between the two polarizations changes significantly: though R-handed emission (red) usually dominates, for a short epoch L-handed emission is stronger in this direction (blue). Critically, we can identify when this transition occurs by comparing our line of sight with the preferred orientation $\hat{V}(t)$ extracted from $\langle \mathcal{L}_a \mathcal{L}_b \rangle$ [26, 27]. Following the discussion above, we expect our calculations confirm (shaded region) that the two polarizations have equal amplitudes (i.e., $|z| = 1$) when $\hat{V} \cdot \hat{n} = 0$, with R-handed emission dominating when $\hat{V} \cdot \hat{n} > 0$ and L-handed emission dominating when $\hat{V} \cdot \hat{n} < 0$. More precisely, we can estimate both the magnitude and phase of z surprisingly reliably by combining Eq. (11) with the orientation $\hat{V}(t)$. For example, the bottom panel of Figure 3 shows the simulated polarization amplitude $|z|$ is

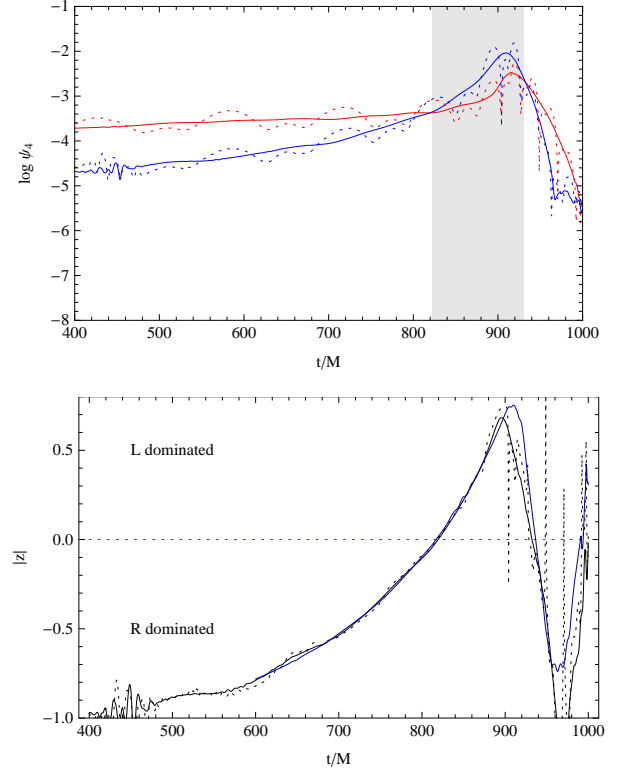


FIG. 3: Polarization imprints on signal 2: Precessing: For a precessing binary, the polarization carries a strong imprint from the relative orientation of the preferred emission direction relative to the line of sight. For the precessing $q = 4$ binary described in the text and [27], a decomposition of the gravitational wave signal along a “generic” orientation $[(\theta, \phi) = (60^\circ, 205^\circ)]$ is shown. Results are shown using just $l = 2$ (solid) and all modes $l \leq 4$ (dotted), *reversing* the convention of Figure 2. *Top panel:* The line of sight right and left-handed amplitudes $|\psi_{4R,L}|$ (red R, blue L) using all modes (dotted) and just $l = 2$ (solid). The gray shaded box shows the interval where $\hat{V} \cdot \hat{n} \leq 0$. *Bottom panel:* Comparison of $|z(t)|$ extracted along this line of sight (black solid [$l = 2$] and dotted curves [$l \leq 4$]) with the leading-order estimate \hat{z}_V provided by Eq. (11) and the preferred orientation \hat{V} selected by $\langle \mathcal{L}_a \mathcal{L}_b \rangle$ (blue).

extremely close to the estimate $|\hat{z}_V|$. Small fluctuations around the leading-order prediction at the orbital period should be due to residual eccentricity.

Despite emphasizing $l = 2$ modes in the discussion above, the inclusion of higher-order angular modes $l \geq 2$ into ψ_4 produces nearly no change to $|z|$. In this example, our naive expression relating z to a preferred direction continues to apply, even when these harmonics produce dramatic fluctuations in the line-of-sight amplitude. Judging from this example, similar calculations for the phase of z , and their repeated success for all lines of sight and simulations considered, we believe z is primarily determined by the orientation of \hat{n} relative to the time-dependent preferred orientation \hat{V} and can usually be well-approximated by Eq. (11).

As described in subsequent sections, our calculations suggest the preferred orientation \hat{V} evolves significantly and rapidly during merger. Equivalently, the polarization content – the distribution of orientations dominated by left versus right handed emission – changes significantly at the merger event. As seen in Figure 4, immediately before and after the merger event, the two points corresponding to predominantly left- or right-handed emission change noticeably. This interval corresponds to the merger phase itself. As described in the next section, we suspect this rapid, global change in polarization content may reflect features of the strong-field merger event itself.

E. Waveforms along other fixed directions

For reference, in Figure 5 we show the polarization content for two other preferred orientations: the initial (\simeq final) total angular momentum direction \hat{J} (top panel) and the preferred orientation \hat{V} evaluated at the time of peak emission (bottom panel). In the first case, one polarization is vastly larger than the other at early times; during the merger, however, both polarizations become significant. Similar results are found when extracting along \hat{z} , the initial orbital angular momentum. In the second case, both polarizations are comparatively large early on. During the merger epoch, however, only one polarization dominates. Generally speaking, when adopting a fixed frame one can choose to simplify some narrow epoch of the waveform by reducing the other polarization. For any time, frequency, or mass range, a generalization of $\langle \mathcal{L}_{(a)\mathcal{L}_{(b)}} \rangle$ can be constructed to determine what orientation would be suitable. However, in general no one orientation works for all time.

Finally, we emphasize that we have been able to accurately estimate the polarization content using the time-dependent preferred orientation \hat{V} . For our simulations, this orientation differs substantially from \hat{L} at all times. Based on this performance, we anticipate that corotating-frame waveforms along \hat{V} will be substantially simpler than any analog extracted along \hat{L} .

III. SIMULATIONS II: TRENDS AND VARIATIONS

From the diagnostics above, we anticipate simulations are best and naturally characterized by (a) the modal waveforms ψ_{4lm} in a corotating frame and (b) the evolution of our preferred orientation with time. In addition, to simplify the translation between time and frequency domain, we will also use (c) the overall orientation-averaged signal power $\bar{\rho}$. In this section we briefly report on salient ways these three features change with spin and mass ratio.

A. Polarization bias

Generic precessing binaries exhibit a *polarization bias*: at any given instant, the binary is radiating more of one handedness than another. During the inspiral, the balance between L and R oscillates. At merger, the balance fixes, preferring one handedness, with the choice depending on the spin-orbit configuration just prior to merger. As described in Healy et al (in prep), this asymmetry produces large kicks, with a significant component perpendicular to the orbital plane; cf. [42].

For the purposes of this paper, this asymmetry complicates our interpretation of the preferred direction. As with nonprecessing binaries, we use the ratio of left to right-handed power to estimate an (instantaneous) *inclination*. The expressions that we invert for $\hat{O} \cdot \hat{n}$ [e.g., Eq. (11)] *assume* an equal amount of left and right handed power. More refined estimates that relate the line of sight to the left/right ratio are required when a strong bias towards one or the other handedness occurs.

To assess whether more complicated expressions would be required in parameter estimation,⁷ we define polarized analogs of the orientation-averaged signal amplitude $\bar{\rho}$ [43], starting from ρ^2 [Eq. (3)]:

$$\bar{\rho}^2 \equiv \int \frac{d\Omega}{4\pi} \rho^2(\hat{n}) = \int \frac{d\Omega}{4\pi} 2 \frac{df}{S_h} \frac{|\psi_4(f, \hat{n})|^2}{(2\pi f)^4} \quad (14)$$

$$\bar{\rho}_R^2 \equiv \int \frac{d\Omega}{4\pi} 2 \int_0^\infty \frac{df}{S_h} \frac{|\psi_4(f, \hat{n})|^2}{(2\pi f)^4} \quad (15)$$

$$\bar{\rho}_L^2 \equiv \int \frac{d\Omega}{4\pi} 2 \int_{-\infty}^0 \frac{df}{S_h} \frac{|\psi_4(f, \hat{n})|^2}{(2\pi f)^4} \quad (16)$$

Any given binary has directions where one polarization dominates (e.g. along \hat{L} for a nonprecessing binary). Summing over all orientations, however, nonprecessing binaries emit symmetrically, with matching amounts of R and L handed emission along mirror-symmetry-related lines of sight. With equal amounts of signal power, nonprecessing binaries must have $\bar{\rho}_L = \bar{\rho}_R = \bar{\rho}/\sqrt{2}$. By contrast, precessing binaries have no symmetry that enforces symmetric emission; particularly in narrow epochs or frequency intervals selected by an outside observer or gravitational wave detector, one handedness (R or L) can dominate. As Figure 6 demonstrates with a specific example and Figure 7 with an ensemble, generally a single polarization does dominate during merger. The dominant polarization depends sensitively on the spins, particularly when S_1, S_2 are nearly antiparallel and in the orbital plane.

⁷ We illustrate polarization asymmetry using a detection-weighted diagnostic to demonstrate the bias is *detectable*. Alternatively and in a detector-agnostic way, the polarization asymmetry also shows up clearly in $(\int d\Omega |\psi_R(\hat{n})|^2) / (\int d\Omega |\psi_L(\hat{n})|^2)$, where the numerator and denominator are evaluated at each time or each frequency.

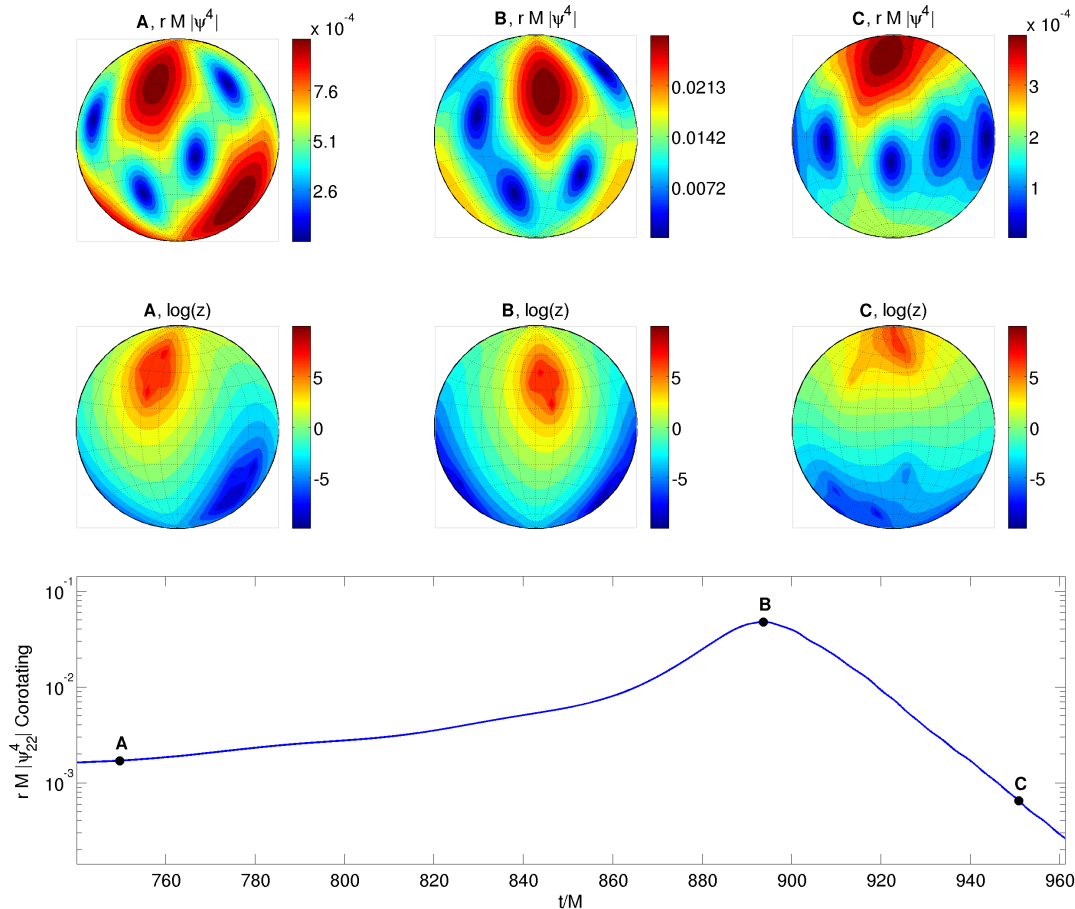


FIG. 4: **Evolution of amplitude, polarization at merger:** Three snapshots of $|\psi_4|$ (top panel) and $|z|$ (bottom panels) for the Sq(4,0.6,90,9) simulation, bracketing the time of peak amplitude and demonstrating that the polarization content changes significantly during the merger event. For aesthetic reasons, we only show the contributions from all $l = 2$ modes.

Our calculations suggest that $\simeq 30\%$ changes in the overall amplitude ($\bar{\rho}$ or ψ_4) are not uncommon during merger. The *relative* amplitude of left to right handed radiation (ρ_R/ρ_L or z), however, changes by orders of magnitude due to small changes in inclination; see Eq. (11) and Figure 3. As a result, the typical polarization bias introduces a fairly small systematic error into any procedure to reconstruct the evolution of \hat{V} [e.g., into the inverse of Eq. (11) for the inclination as a function of time].

B. Corotating waveforms, chirality

The corotating-frame waveforms will be described in detail in a subsequent publication. For the purposes of this paper, we will employ only two key features. First and foremost, like their nonprecessing analogs, the corotating frames are *chiral*: modes with $m > 0$ have frequency content only for $f > 0$ and vice-versa. We can quantify how precisely we are confident that the

modes are chiral in a way that is relevant to data analysis. For example, we can decompose the contribution of each *corotating* mode to *fictitious*⁸ “orientation-averaged signal-to-noise ratios” $\bar{\rho}_{R,L}$ associated with each handedness:

$$\bar{\rho}_{lm,R,corot}^2 \equiv \frac{1}{4\pi} 2 \int_0^\infty \frac{df}{S_h} \frac{|\psi_{4,lm}^{corot}(f)|^2}{(2\pi f)^4} \quad (17)$$

$$\bar{\rho}_{lm,L,corot}^2 \equiv \frac{1}{4\pi} 2 \int_{-\infty}^0 \frac{df}{S_h} \frac{|\psi_{4,lm}^{corot}(f)|^2}{(2\pi f)^4} \quad (18)$$

Applying these expressions, we find $\bar{\rho}_{lm,L}/\bar{\rho}_{lm} \simeq 0$ for $m > 0$: modes that should have positive helicity ($m > 0$) have little negative-frequency power. As a corollary, the corotating-frame $(2, 2)$ and $(2, -2)$ modes are *nearly orthogonal* – as, more generally, are the subspaces spanned

⁸ Fictitious since they are associated with a corotating frame.

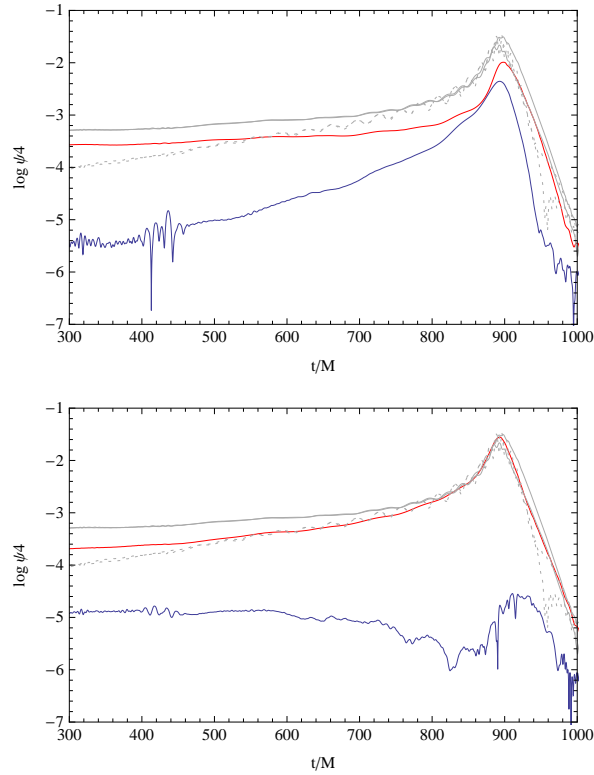


FIG. 5: Polarization content along fixed special directions: The right- and left-handed Weyl scalar amplitude $|\psi_{4R,L}|$ (red, blue) versus time, for the gravitational wave signal extracted along several preferred orientations. For comparison, the gray lines show the simulation-frame $(2, \pm 2)$ (solid gray) and $(2, \pm 1)$ modes (dotted gray). For aesthetic reasons, we only show the contributions from the $l = 2$ modes. *Top panel:* Initial total angular momentum. *Bottom panel:* \hat{V} at the time of peak emission. From the ratio of left to right (blue to red), the direction identified by \hat{V} corresponds to nearly circular polarization near the epoch of peak emission. This direction is significantly offset from \hat{J} .

by modes with $m > 0$ and $m < 0$. We will use the orthogonality of the corotating-frame $(2, 2)$ and $(2, -2)$ modes to model how precisely we can measure the orientation of the corotating frame, both on average and as function of time.

C. Preferred direction precesses

For the simulations and time intervals we have simulated, the preferred orientation \hat{V} evolves as if precessing along a nearly-constant cone, centered along some axis \hat{W} . Figure 8 provides a concrete example. In almost all cases we find $\hat{W} \simeq \hat{J}_{\text{final}}$ empirically: \hat{V} precesses around the total angular momentum. For this section only, however, we allow \hat{W} to take arbitrary values.

Given that orientation and an arbitrary frame \hat{x}_W, \hat{y}_W defined perpendicular to the constant vector \hat{W} , we define the precession phase ϕ_W and precession frequency

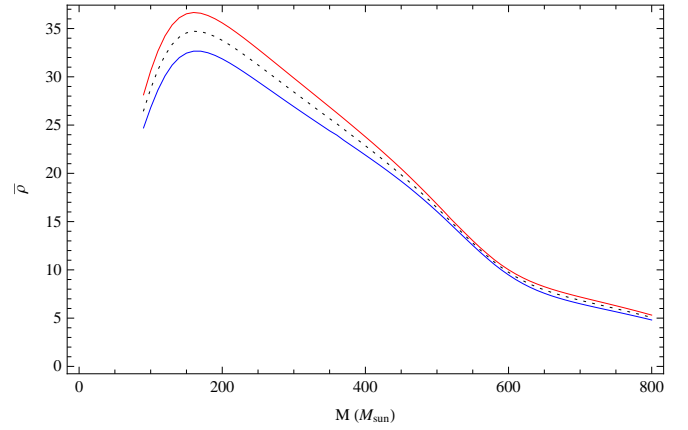


FIG. 6: Merger signals are polarized overall: Depending on the spins, binary black holes can emit substantially more L or R handed power. As an example, a comparison of $\bar{\rho}_R$ (red) and $\bar{\rho}_L$ (blue) to $\bar{\rho}/\sqrt{2}$ (dotted) for a binary starting with $a_1 = a\hat{n}(60^\circ)$, $a_2 = a\hat{z}$. In this expression we adopt a fiducial initial LIGO design noise curve.

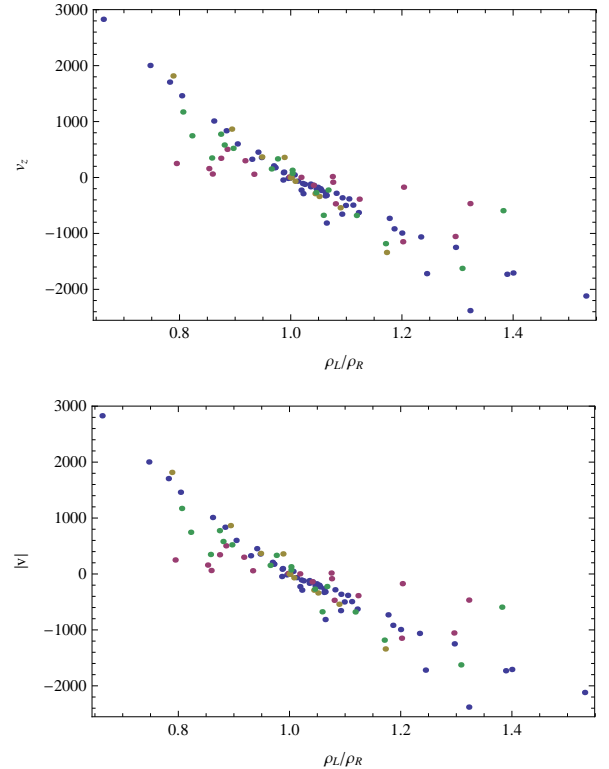


FIG. 7: Large L/R asymmetries and large kicks: Scatter plot of the recoil kick velocity in the \hat{z} direction (top panel) and overall (bottom panel) versus $\bar{\rho}_L/\bar{\rho}_R$. Large kicks in the $+\hat{z}$ direction correlate with predominantly L -handed emission. The largest possible kicks, however, correspond to fairly moderate asymmetries between L and R during merger. In this figure, colors correspond to different simulation sets: S (blue), Sq (red), T (yellow), Tq (green). For illustrating the correlation between R vs L bias and kick magnitude only: kick data is computed using the simulation series alone at a single extraction radius, without correcting for the early inspiral.

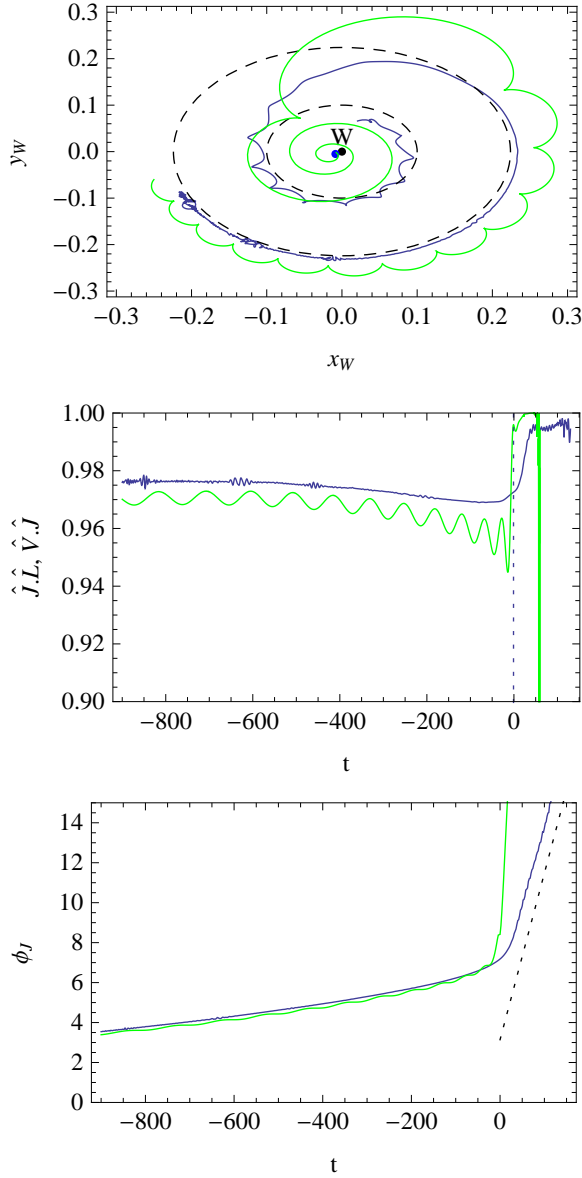


FIG. 8: **Precession of preferred orientation: Example:** Demonstration that the preferred orientation precesses around $\hat{W} \simeq \hat{J}$ for $q = 2, d = 10M, a_1 = 0.6\hat{x}, a_2 = 0.6\hat{z}$. *Top panel:* Two-dimensional path of V (blue) and \hat{L} (green) around a proposed value of W (point at origin), as seen in a plane perpendicular to \hat{W} . The two dashed curves are circles of constant opening angle. For comparison, a blue point indicates the final angular momentum direction \hat{J} in this frame. *Center panel:* $\hat{J} \cdot \hat{V}$ (blue) and $\hat{J} \cdot \hat{L}$ (green), showing both \hat{L} and \hat{V} precess along similar cones, with a nearly constant opening angle prior to merger. In this figure, merger occurs at $t \simeq 0$. *Bottom panel:* Plot of ϕ_W before and after merger, demonstrating an abrupt change in the precession frequency at the merger event. For comparison, the green curve shows ϕ_L , the precession phase extracted from L around J . For this system, at late times the “precession rate” $\Omega_{VW} \equiv \partial_t \phi_W \simeq 1/12M$ is still an order of magnitude smaller than $\partial_t \Phi$, the “carrier frequency” set by the $(2, 2)$ and $(2, -2)$ modes.

Ω_{VW} via

$$e^{i\phi_{VW}} = \frac{(\hat{x}_W + i\hat{y}_W) \cdot \hat{V}}{|(\hat{x}_W + i\hat{y}_W) \cdot \hat{V}|} \quad (19a)$$

$$\Omega_{VW} = \partial_t \phi_W \quad (19b)$$

and make similar definitions for \hat{L} around \hat{J} . During the inspiral, the two vectors \hat{V} and \hat{L} nearly coincide, precessing around a similar center at a similar rate. To quantify this similarity, Figure 8 shows the opening angle of each precession cone ($\hat{J} \cdot \hat{L}$ and $\hat{J} \cdot \hat{V}$) and the “phase” ϕ_{VJ} and ϕ_{LJ} of the vectors \hat{L} and \hat{V} as they precess around \hat{J} . Prior to merger, both quantities largely agree.

As the binary plunges and merges, the precession cones of both \hat{L} and \hat{V} cycle around their respective axes (\hat{J} and \hat{W}) at a higher rate. By comparison to \hat{L} , however, the preferred axis \hat{V} has a much smaller precession rate and persists in precession cycles long after merger. Furthermore, contrary to our intuition, the opening angle of the precession cone for \hat{V} (i.e., $\arccos(\hat{W} \cdot \hat{V})$) rarely decays significantly after merger. This precession cycle of \hat{V} is robust: both for this simulation and all others tested, all extraction radii and (when available) all resolutions show quantitatively similar features.

For each simulation, we estimated \hat{W} and ϕ_W by fitting a fixed precession cone to the trajectory of \hat{V} . Specifically, we adopt as \hat{W} the direction that minimizes the rms difference between $V(t) \cdot \hat{W}$ and its time average. This choice corresponds to the assumption that the precession cone swept out by \hat{V} should have a constant opening angle. When estimating \hat{W} , we separately fit data *prior to merger* and *after merger*. In almost all cases we found $\hat{W} \simeq \hat{J}$ and $\Omega_{VJ} \simeq \Omega_{VW}$.

To further demonstrate the close correspondence between these two directions, Figure 9 shows *both* angular frequencies: points appear at the median value $(\Omega_{VW} + \Omega_{VJ})/2$; the bar has height $\pm(\Omega_{VW} + \Omega_{VJ})/2$. Except for a handful of cases, mostly associated with nearly-aligned spins, these two expressions agree. We conservatively adopt the difference $(\Omega_{VW} - \Omega_{VJ})/2$ as an estimate of our systematic error. [Other sources of systematic error, such as extraction radius, have a smaller effect on the recovered post-merger precession rate.]

D. Post-merger precession 1: Results

In our simulations, if the binary precesses *prior* to merger, our preferred direction \hat{V} continues to precess *after* merger, never converging towards \hat{J} . Precession is ubiquitous (i.e., whenever \hat{L} and \hat{J} are initially misaligned); we therefore expect ubiquitous precession-induced modulations at and after merger when asymmetric binaries merge with randomly-oriented spins. As described in a companion publication, we have performed extensive resolution tests and remain confident that the post-merger oscillations we observe are resolved. Table I

provides an estimate of the post-merger “precession frequencies” Ω_{VJ} for each of our simulations.

Figure 9 demonstrates that the post-merger “precession” frequencies are principally determined by the final black hole’s spin magnitude. Because the final black hole can be described as a superposition of quasinormal modes, the precession frequencies are very nearly *differences* between the $(l, m) = (2, 2)$ and $(2, 1)$ quasinormal modes of the remnant hole [44]; see Figure 9.

By some change of basis, the long-lived post-merger oscillations must be described as some perturbation of the final remnant black hole: a (coherent) superposition of multiple quasinormal modes. Our calculations suggest precessing mergers coherently excite multiple quasinormal modes of different angular order. These quasinormal modes have similar decay timescales ($1/\text{Im}(\omega)$) but noticeably different characteristic frequencies ($1/\text{Re}(\omega)$). As a result, though in principle the quasinormal modes are not *exactly* degenerate, in *practice* just after merger these coherently-excited quasinormal modes decay at a similar rate but with changing relative phase, leading to a black hole state that appears to precess.

To illustrate why our preferred direction precesses, we consider a toy model that approximates features of a superposition of outgoing quasinormal modes:

$$r\psi_{4con}(t) \equiv \sum_m a_{2|m|} e^{-i\omega_{lm}t} Y_{lm}^{(-2)} \quad (20)$$

where ω_{lm} is the lowest-order eigenfrequency for the (l, m) eigenspace, where the eigenmodes are defined relative to the black hole’s angular momentum direction \hat{J} , and where $a_{2|m|}$ are three real parameters. In this example, we ignore the difference between the actual angular eigenfunctions of the Kerr-background wave equations (spin-weighted spheroidal harmonics) and the corresponding eigenfunctions for flat space, $Y_{lm}^{(-2)}$. In the trivial case where only $a_{2\pm 2}$ are nonzero, the preferred orientation remains along the black hole’s angular momentum axis \hat{J} [45]. Allowing $a_{2\pm 1}$ to be nonzero but keeping $a_{20} = 0$ leads to a preferred orientation \hat{V} that spirals inward exponentially towards \hat{J} , precessing around \hat{z} with a frequency $\Omega_V = \text{Re}(\omega_{22} - \omega_{21})$ and shrinking towards \hat{z} at a different rate $\Gamma_V = \text{Im}(\omega_{22} - \omega_{21})$. Finally, when all mode amplitudes are nonzero, the preferred orientation can exhibit a wide range of behaviors depending on the relative mode ratios a_{21}/a_{22} and a_{20}/a_{22} , including exponential decay to \hat{J} ; modulated precession around \hat{J} ; and pathologically complicated behavior in the presence of degeneracies.

In this interpretation, the angle between \hat{V} and \hat{J} reflects the amplitude of the $(2, \pm 1)$ modes. Conversely, the angle between \hat{V} and \hat{J} is also partially *geometric*, being tied to the spin-orbit configuration and how it the binary evolves during merger. However, as is apparent from Figure 8, the late-time $(2, 1)$ amplitude (i.e., the angle $V \cdot J$) *evolves* during the strong-field merger event. We anticipate the opening angle provides new insight into the strong-field merger process.

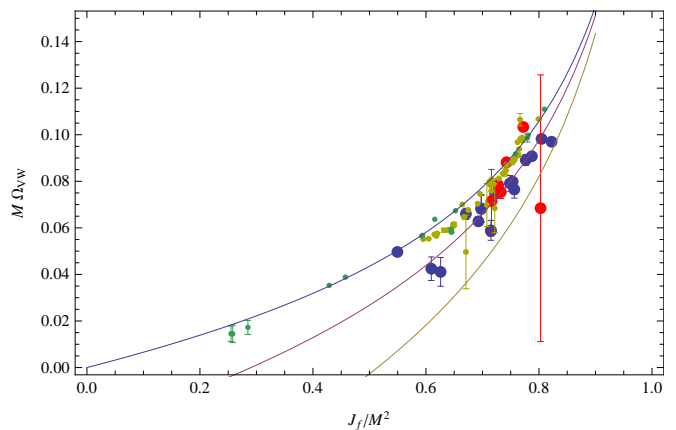


FIG. 9: **Post-merger precession frequency:** For each of the simulations listed in Table I, a scatterplot of their “post-merger precession frequency” $M_f \Omega_{VW}$ [Eq. (19)] against the final black hole’s spin magnitude J_f/M_f^2 . Colors indicate four different classes of simulation: Tq (blue), T (red), Sq (green) and S (yellow). For comparison, the solid lines show the quasinormal mode frequency differences $\omega_{122} - \omega_{121}$ (blue) and $\omega_{222} - \omega_{221}$ (yellow), where ω_{nlm} is the real part of the quasinormal eigenfrequency [44]. The bars indicate differences between two methods for estimating Ω ; see Section III C.

E. Post-merger precession 2: Broader context

Our results suggest that the nonlinear merger event coherently seeds multiple quasinormal modes. After merger, all quasinormal modes appear to precess almost coherently, in a frame aligned with the final black hole’s spin. For example, each constant- l subspace seems to precess at a similar rate. We defer a detailed discussion of each constant- l subspace to subsequent publications.

Our results agree with a recently-developed geometric interpretation of Kerr quasinormal modes. Using a short-wavelength limit, Yang et al. [28] recently showed that these kinds of quasinormal mode frequency differences are intimately connected to precession of spherical photon orbits. Our calculations suggest this kind of geometric interpretation holds even in the strong field, during merger.

Because rapid polarization changes occur during the merger epoch, we anticipate that these polarization changes encode linear and potentially nonlinear features of strong-field gravity. At a minimum, the precession cycle of \hat{V} persists during and after the merger, with a precession rate tied to the quasinormal mode frequency distribution of the final hole. Modulations in the line of sight polarization content provide a natural way to identify this characteristic frequency, potentially allowing new experimental tests of general relativity. Second, the long-term, multimodal coherence we observe suggests a short, nonlinear, and nontrivial process seeds a coherent multimodal perturbation of the final black hole. In part, of course, the perturbed black hole simply inherits its features from the just-prior-to-merger binary. In the

Key	r_{start}	q	$S_{1,x}/M^2$	$S_{1,y}/M^2$	$S_{1,z}/M^2$	$S_{2,x}/M^2$	$S_{2,y}/M^2$	$S_{2,z}/M^2$	$\bar{\rho}_L/\bar{\rho}_R$	Ω_{VJ}	T/M	T_{wave}/M	M/h
Sq(2,0.6, 0,6.2)	6.2	2	0.	0.	0.2666	-0.0666	0.	0.	1.11	0.12	599.	342.5	140
Sq(2,0.6,30,6.2)	6.2	2	0.1333	0.	0.2309	-0.0666	0.	0.	1.29	0.11	548.	326.3	140
Sq(2,0.6,90,6.2)	6.2	2	0.2666	0.	0.	-0.0666	0.	0.	0.83	0.07	411.	255.1	140
Sq(2,0.6,150,6.2)	6.2	2	0.1333	0.	-0.2309	-0.0666	0.	0.	1.03	0.04	415.2	195.4	140
Sq(2,0.6,180,6.2)	6.2	2	0.	0.	-0.2666	-0.0666	0.	0.	0.86	0.37	396.6	187.8	140
Sq(2,0.6,270,6.2)	6.2	2	-0.2666	0.	0.	-0.0666	0.	0.	1.31	0.08	497.9	267.5	140
Sq(4,0.6, 0, 6.2)	6.2	4	0.	0.	0.384	-0.024	0.	0.	0.99	0.10	583.2	434.5	140
Sq(4,0.6,30,6.2)	6.2	4	0.192	0.	0.3325	-0.024	0.	0.	1.13	0.095	599.	427.1	140
Sq(4,0.6,90,6.2)	6.2	4	0.384	0.	0.	-0.024	0.	0.	0.96	0.058	549.9	264.6	140
Sq(4,0.6,150,6.2)	6.2	4	0.192	0.	-0.3325	-0.024	0.	0.	1.06	0.01	408.1	165.6	140
Sq(4,0.6,180,6.2)	6.2	4	0.	0.	-0.384	-0.024	0.	0.	0.91	-	415.5	165.6	140
Sq(4,0.6,270,6.2)	6.2	4	-0.384	0.	0.	-0.024	0.	0.	0.77	0.07	549.9	280.6	140
Sq(4,0.6,0,9)	9.	4	0.	0.	0.384	-0.024	0.	0.	1.06	0.05-0.1	1599.	1273.1	140
Sq(4,0.6,90,9)	9.	4	0.384	0.	0.	-0.024	0.	0.	0.76	0.058	1194.4	867.	140
Sq(4,0.6,150,9)	9.	4	-0.192	0.	-0.3325	-0.024	0.	0.	1.20	0.01	799.	487.5	140
Sq(4,0.6,180,9)	9.	4	0.	0.	-0.384	-0.024	0.	0.	1.1	-	799.	426.1	140
Sq(4,0.6,210,9)	9.	4	0.192	0.	-0.3325	-0.024	0.	0.	0.77	0.014	797.5	464.	140
Sq(4,0.6,270,9)	9.	4	-0.384	0.	0.	-0.024	0.	0.	1.37	0.06	1138.7	883.2	140
T(1,0,2,45)	10	1	0.	0.	0.05	0.0354	0.	0.0354	1.05	0.087	1298.9	849.	77
T(1,0,2,60)	10	1	0.	0.	0.05	0.0433	0.	0.025	1.07	0.08	1298.9	837.	77
T(1,0,2,90)	10	1	0.	0.	0.05	0.05	0.	0.	1.03	0.07-0.1	1298.9	838.2	77
T(1,0,4,45)	10	1	0.	0.	0.1	0.0707	0.	0.0707	0.96	0.1	1499.	986.6	77
T(1,0,4,60)	10	1	0.	0.	0.1	0.0866	0.	0.05	0.86	0.1	1499.	965.8	77
T(1,0,4,90)	10	1	0.	0.	0.1	0.1	0.	0.	1.07	0.11	1499.	908.3	77
T(1,0,6,45)	10	1	0.	0.	0.15	0.1061	0.	0.1061	0.92	0.11	1499.	1052.1	77
T(1,0,6,60)	10	1	0.	0.	0.15	0.1299	0.	0.075	1.2	0.12	1499.	993.7	77
T(1,0,6,90)	10	1	0.	0.	0.15	0.15	0.	0.	0.73	0.1	1499.	915.7	77
T(1,0,0)	10	1	0.	0.	0.	0.	0.	0.	1	-	1099.	885.5	77
T(1,0,2,0)	10	1	0.	0.	0.05	0.	0.	0.05	1	-	1298.9	906.4	77
T(1,0,4,0)	11	1	0.	0.	0.1	0.	0.	0.1	1	-	1398.9	997.5	77
T(1,0,6,0)	10	1	0.	0.	0.15	0.	0.	0.15	1	-	1499.	1086.	77
T(1,0,8,0)	10	1	0.	0.	0.2	0.	0.	0.2	1	-	1699.	1217.7	77
Tq(1.5,0.4,60)	10	1.5	0.1247	0.	0.072	0.	0.	0.064	0.95	0.085	1498.9	1157.7	120
Tq(1.5,0.6,45)	10	1.5	0.1527	0.	0.1527	0.	0.	0.096	1.17	0.11	1598.9	1298.8	120
Tq(1.5,0.6,60)	10	1.5	0.187	0.	0.108	0.	0.	0.096	1.2	0.10	1598.9	1251.9	120
Tq(1.5,0.6,90)	10	1.5	0.216	0.	0.	0.	0.	0.096	1.34	0.07	1598.8	1134.1	120
Tq(2,0.4,60)	10	2	0.1539	0.	0.0889	0.	0.	0.0444	0.91	0.08	1598.9	1216.1	120
Tq(2,0.6,45)	10	2	0.1885	0.	0.1885	0.	0.	0.0666	0.90	0.106	1698.9	1390.9	120
Tq(2,0.6,60)	10	2	0.2309	0.	0.1333	0.	0.	0.0666	0.88	0.095	1698.9	1328.4	120
Tq(2,0.6,90)	10	2	0.2666	0.	0.	0.	0.	0.0666	0.72	0.075	1598.9	1176.4	120
Tq(2.5,0.4,45)	10	2.5	0.1443	0.	0.1443	0.	0.	0.0326	0.85	0.06	1698.9	1351.6	120
Tq(2.5,0.4,60)	10	2.5	0.1767	0.	0.102	0.	0.	0.0326	1.03	0.06	1598.9	1297.6	120
Tq(2.5,0.4,90)	10	2.5	0.2041	0.	0.	0.	0.	0.0326	0.79	0.04	1498.9	1180.4	120
Tq(2.5,0.6,45)	10	2.5	0.2164	0.	0.2165	0.	0.	0.049	0.94	0.095	1798.9	1488.4	120
Tq(2.5,0.6,60)	10	2.5	0.2651	0.	0.1531	0.	0.	0.049	1.24	0.076	1798.9	1409.6	120
Tq(2.5,0.6,90)	10	2.5	0.3061	0.	0.	0.	0.	0.049	1.14	0.066	1598.9	1226.4	120
Tq(4, 0.6, 45)	10	4	0.2715	0.	0.2715	0.	0.	0.024	0.88	0.078	2198.9	1805.7	120
Tq(4, 0.6, 60)	10	4	0.3325	0.	0.192	0.	0.	0.024	0.90	0.058	1998.9	1698.1	120
Tq(4, 0.6, 90)	10	4	0.384	0.	0.	0.	0.	0.024	1.4	0.038	1798.9	1420.	120
S(1,0,2,0)	6.2	1	0	0	0.05	-0.05	0	0	0.95		392	250	77
S(1,0,2,45)	6.2	1	0.0354	0.	0.0354	-0.05	0.	0.	0.96	unk	380.7	246.6	77
S(1,0,2,90)	6.2	1	0.05	0.	0.	-0.05	0.	0.	1.04	unk	389.2	217.4	77
S(1,0,2,135)	6.2	1	0.0354	0.	-0.0354	-0.05	0.	0.	1.11	0.55	394.9	206.9	77
S(1,0,2,180)	6.2	1	0.	0.	-0.05	-0.05	0.	0.	1	0.07	394.9	210.8	77
S(1,0,2,225)	6.2	1	-0.0354	0.	-0.0354	-0.05	0.	0.	1.03	0.07	389.2	207.9	77
S(1,0,2,270)	6.2	1	-0.05	0.	0.	-0.05	0.	0.	1	0.08	383.2	221.8	77
S(1,0,2,315)	6.2	1	-0.0354	0.	0.0354	-0.05	0.	0.	0.98	0.08	384.	247.6	77
S(1,0,4,0)	6.2	1	0.	0.	0.1	-0.1	0.	0.	0.86	0.09	398.9	277.3	77
S(1,0,4,45)	6.2	1	0.0707	0.	0.0707	-0.1	0.	0.	0.8	-	398.9	264.5	77
S(1,0,4,90)	6.2	1	0.1	0.	0.	-0.1	0.	0.	1.09	-	398.9	227.1	77
S(1,0,4,135)	6.2	1	0.0707	0.	-0.0707	-0.1	0.	0.	1.29	0.055	398.9	209.8	77
S(1,0,4,180)	6.2	1	0.	0.	-0.1	-0.1	0.	0.	1.15	0.07	398.9	208.7	77
S(1,0,4,225)	6.2	1	-0.0707	0.	-0.0707	-0.1	0.	0.	1.06	0.07	398.9	209.6	77
S(1,0,4,270)	6.2	1	-0.1	0.	0.	-0.1	0.	0.	1	0.08	398.9	240.8	77
S(1,0,4,315)	6.2	1	-0.0707	0.	0.0707	-0.1	0.	0.	0.94	0.09	398.9	274.2	77
S(1,0,6,0)	6.2	1	0.	0.	0.15	-0.15	0.	0.	1.07	0.1	398.9	289.7	77
S(1,0,6,15)	6.2	1	0.0388	0.	0.1449	-0.15	0.	0.	0.95	0.1	498.9	288.7	77
S(1,0,6,30)	6.2	1	0.075	0.	0.1299	-0.15	0.	0.	0.80	0.1	498.9	276.7	77
S(1,0,6,45)	6.2	1	0.1061	0.	0.1061	-0.15	0.	0.	0.69	0.1	498.9	270.5	77
S(1,0,6,60)	6.2	1	0.1299	0.	0.075	-0.15	0.	0.	0.69	-	498.9	263.3	77
S(1,0,6,75)	6.2	1	0.1449	0.	0.0388	-0.15	0.	0.	0.84	0.08	498.9	248.2	77
S(1,0,6,90)	6.2	1	0.15	0.	0.	-0.15	0.	0.	1.15	-	398.9	229.8	77
S(1,0,6,105)	6.2	1	0.1449	0.	-0.0388	-0.15	0.	0.	1.44	0.07	498.9	200.5	77
S(1,0,6,120)	6.2	1	0.1299	0.	-0.075	-0.15	0.	0.	1.51	0.05	498.9	211.	77
S(1,0,6,135)	6.2	1	0.1061	0.	-0.1061	-0.15	0.	0.	1.41	0.06	498.9	206.9	77
S(1,0,6,150)	6.2	1	0.075	0.	-0.1299	-0.15	0.	0.	1.27	0.06	498.9	202.1	77
S(1,0,6,165)	6.2	1	0.0388	0.	-0.1449	-0.15	0.	0.	1.15	0.06	498.9	198.6	77
S(1,0,6,180)	6.2	1	0.	0.	-0.15	-0.15	0.	0.	1.09	0.06	498.9	198.4	77
S(1,0,6,195)	6.2	1	-0.0388	0.	-0.1449	-0.15	0.	0.	1.07	0.06	498.9	199.8	77
S(1,0,6,210)	6.2	1	-0.075	0.	-0.1299	-0.15	0.	0.	1.07	0.06-0.07	498.9	204.6	77
S(1,0,6,225)	6.2	1	-0.1061	0.	-0.1061	-0.15	0.	0.	1.08	0.07	498.9	206.5	77
S(1,0,6,240)	6.2	1	-0.1299	0.	-0.075	-0.15	0.	0.	1.07	0.07	498.9	204.	77
S(1,0,6,255)	6.2	1	-0.1449	0.	-0.0388	-0.15	0.	0.	1.04	0.08	495.6	233.1	77
S(1,0,6,260)	6.2	1	-0.1477	0.	-0.026	-0.15	0.	0.	1.03	0.08	498.9	248.	77
S(1,0,6,265)	6.2	1	-0.1494	0.	-0.0131	-0.15	0.	0.	1.02	0.085	498.9	251.3	77
S(1,0,6,270)	6.2	1	-0.15	0.	0.	-0.15	0.	0.	1	0.09	436.7	254.4	77
S(1,0,6,285)	6.2	1	-0.1449	0.	0.0388	-0.15	0.	0.	0.97	0.09	488.4	274.2	77
S(1,0,6,300)	6.2	1	-0.1299	0.	0.075	-0.15	0.	0.	0.99	0.11	498.9	279.2	77
S(1,0,6,315)	6.2	1	-0.1061	0.	0.1061	-0.15	0.	0.	1.03		498.9	287.7	77
S(1,0,6,330)	6.2	1	-0.075	0.	0.1299	-0.15	0.	0.	1.08	0.1	498.9	289.5	77
S(1,0,6,345)	6.2	1	-0.0388	0.	0.1449	-0.15	0.	0.	1.1	0.1	498.9	290.2	77
S(1,0,8,0)	6.2	1	0.	0.	0.2	-0.2	0.	0.	1.5	0.12	498.9	306.1	77
S(1,0,8,30)	6.2	1	0.1	0.	0.1732	-0.2	0.	0.	1.24	0.11	498.9	292.8	77
S(1,0,8,60)	6.2	1	0.1732	0.	0.1	-0.2	0.	0.	0.59	0.097	498.9	269.1	77
S(1,0,8,90)	6.2	1	0.2	0.	0.	-0.2	0.	0.	1.09	-	498.9	232.7	77
S(1,0,8,120)	6.2	1	0.1732	0.	-0.1	-0.2	0.	0.	1.70	0.062	498.9	210.6	77
S(1,0,8,150)	6.2	1	0.1	0.	-0.1732	-0.2	0.	0.	1.17	0.061	498.9	195.3	

geometric point of view, $\hat{V} \cdot \hat{J} \neq 0$ prior to merger; in the quasinormal mode view, the $(2, 1)$ mode just prior to plunge partially limits the $(2, 1)$ quasinormal mode amplitude during and after merger. However, the merger process partially but *incompletely* sheds this quantity. We anticipate that the amplitude of this effect, measured either by $\hat{V} \cdot \hat{J}$ or the peak $(2, 1)$ amplitude in a frame aligned with \hat{J} , will provide a useful probe of the strong-field merger process.

F. Recovering the direction using polarization

For precessing binaries, we have argued that the line-of-sight polarization, as a function of time, determines both the line of sight and the path of \hat{V} , a preferred direction. We have argued this process works for all time, both prior to and after merger. In the theorists' paradise – access to a noise-free line-of-sight signal $\psi_4(t)$ – we have already arrived at this paper's key result: by tracking polarization, we can partially reconstruct properties of the source binary, even when limited to the short merger epoch.

In practice, however, gravitational wave detectors have limited sensitivity, with access to only a small time and frequency interval of the full signal. Nonetheless, as we argue below, both the polarization bias, $\bar{\rho}_L/\bar{\rho}_R$, and preferred orientation, \hat{V} , can be *measured* by tracking the time-dependent polarization along a single line of sight.

IV. POLARIZATION IS MEASURABLE

In the previous section we described how to characterize the polarization content of a gravitational wave signal. In this section we demonstrate that this content is experimentally accessible, both on average and to a lesser extent as a function of time. We quantify the amount of polarization difference that experiments can distinguish. In particular, we show how fairly small polarization fluctuations can lead to substantial differences between nonprecessing and precessing waveforms.

A. Nonprecessing binaries

As shown above [Eq. (10)], for nonprecessing binaries measurements of the polarization content z are equivalent to constraints on the emission inclination (θ). While phrased in different coordinates and applied to an entirely different mass regime where semianalytic waveform models exist, several extensive discussions of parameter estimation including inclination exist in the literature [17, 46–52]. For a signal of amplitude ρ , the inclination can be measured to order

$$\Delta(\cos \theta) \simeq 1/\rho$$

Detailed Fisher matrix and Markov-chain Monte Carlo calculations corroborate this simple estimate [17, 46–52].

For nonprecessing binaries dominated by $l = |m| = 2$ emission, the polarization content is equally a measure of the relative amplitude (and phase) of the $(2, 2)$ versus $(2, -2)$ modes; see Eq. (10). Because the $(2, 2)$ and $(2, -2)$ modes have definite (and opposite) helicity, we can equally interpret inclination measurements and polarization content constraints as information about the relative importance of left- and right-handed emission, *averaged over the whole signal*.

B. Static and dynamic polarization content accessible

As demonstrated extensively for nonprecessing signals, gravitational wave observations can constrain the polarization content of a static signal. By implication, observations can equally well constrain the “static part” of a signal with weakly-time-varying polarization content. Generalizing, observations should also be able to constrain some “average polarization” from an arbitrary gravitational wave signal. How? Conceptually, gravitational wave detector networks can be arranged to be sensitive to only one (circular or linear) polarization at a time. By measuring the total power incident in each polarization, we directly constrain the “average polarization.”

A detailed analysis of the response of real gravitational wave detector networks to each circular polarization is beyond the scope of this paper. Instead, for simplicity and following the philosophy outlined in [27] and near Eq. (3), we will idealize gravitational wave networks as equally sensitive to both linear polarizations. By construction, the left- and right-handed components of ψ_4 are orthogonal. The net signal amplitude ρ^2 can be expressed as a sum of left- and right-handed components:

$$\rho_R^2 \equiv 2 \int_0^\infty \frac{df}{S_h} \frac{|\psi_4(f, \hat{n})|^2}{(2\pi f)^4} \quad (21)$$

$$\rho_L^2 \equiv 2 \int_{-\infty}^0 \frac{df}{S_h} \frac{|\psi_4(f, \hat{n})|^2}{(2\pi f)^4} \quad (22)$$

Observations determine the integrated contributions from both polarizations ($\rho_{R,L}$) independently. In this averaged sense, observations can unambiguously determine the polarization content: we can simply measure the (source mass and detector-dependent) ratio

$$\bar{z}(M) \equiv \rho_L/\rho_R. \quad (23)$$

For nonprecessing binaries, the average polarization amplitude corresponds precisely to the instantaneous polarization amplitude given in Eq. (10). Motivated by the accuracy of inclination measurements and fluctuations in each (independent) polarization, we anticipate this quantity can be measured to order $\Delta \ln z \simeq 1/\min(\rho_R, \rho_L)$.

For sufficiently strong signals, the Weyl scalar can be reconstructed in the time domain, allowing us to estimate $\psi_{4R,L}$ and therefore the polarization content at each time. Nonparametric signal reconstruction algorithms like **coherent waveburst** are already employed in attempts to identify and reconstruct signals from unmodeled sources [53, 54]. At the signal amplitudes expected from the first merger detections, however, fully nonparametric models generally have too much freedom to tightly constrain the polarization evolution seen in merging black hole binaries. Nonetheless, tighter constraints should be achievable, to the extent that precession-related timescales remain long compared to other scales in the signal.

In fact, several post-Newtonian parameter estimation studies have demonstrated how well these longer timescales can be constrained and differentiated, using both ground- and space-based interferometers [49, 51, 52]. Implicitly, the initial conditions of an inspiralling, precessing binary encode its precession trajectory, albeit in suboptimal coordinates.⁹ To the extent that post-Newtonian study of binary parameter estimation confirm both spins and directions of merging binaries can be measured, they also imply the (time-dependent) precession trajectory can be distinguished. Furthermore, post-Newtonian simulations suggest that even marginal precession (i.e., even less than one precession cycle) has a dramatic impact: if precession is included, then precessing signals can appear dramatically different than their similar nonprecessing counterparts.

C. Polarization-induced mismatch: Loss of amplitude relative to nonprecessing

To demonstrate the critical impact even weak but *time-dependent* precession has on a merger signal, we remove it. Specifically, we start with our standard precessing binary, examine all possible emission directions, and determine how well a comparable nonprecessing analog could fit them. To reduce ambiguity, for our “nonprecessing” analog we use the *corotating-frame* $(2, \pm 2)$ modes from that same simulation.¹⁰ The procedure for constructing these waveforms is described in a companion publication

[55]. As noted above, these two corotating modes are orthogonal, with support only for $f > 0$ or $f < 0$ respectively. Specifically, a nonprecessing analog of our binary would be well-approximated by any linear combination of the $(2, 2)$ and $(2, -2)$ modes.

As in our prior work [26, 27], for simplicity we compare two complex waveforms using an inner product that accounts for both polarizations simultaneously:

$$(A, B) \equiv \int_{-\infty}^{\infty} 2 \frac{\tilde{A}(f)^* \tilde{B}(f)}{(2\pi f)^4 S_h} df \quad (24)$$

In this expression we are not maximizing over time or phase. Using this inner product, we can define two normalized L and R-handed basis states from the corotating-frame modes:

$$|R\rangle = \psi_{422}(t) / \sqrt{(\psi_{422}, \psi_{422})} \quad (25)$$

$$|L\rangle = \psi_{42-2}(t) / \sqrt{(\psi_{42-2}, \psi_{42-2})} \quad (26)$$

Using these orthonormal basis states, we can construct the “nonprecessing signal” ψ_{est} that best resembles $\psi(t, \hat{n})$:

$$|\psi_{est}\rangle = (R, \psi) |R\rangle + (L, \psi) |L\rangle \equiv \mathcal{P}\psi \quad (27)$$

where \mathcal{P} is a projection operator to the subspace spanned by R, L . From the difference between this state and the original state, we can determine how much information is lost by a nonprecessing approximation for each candidate line of sight:

$$\rho_{rem}^2 \equiv (\psi, (1 - \mathcal{P})\psi) = \rho^2 - |(R, \psi)|^2 - |(L, \psi)|^2 \quad (28)$$

This expression can be further simplified by expanding ψ in left- and right-handed functions of time along that line of sight:

$$|\psi\rangle \equiv \rho_L |\hat{\psi}_L\rangle + \rho_R |\hat{\psi}_R\rangle = |\hat{\psi}\rangle \rho \quad (29)$$

where for clarity we adopt hats to denote normalized signals (e.g., $|\hat{\psi}\rangle = |\psi\rangle / \rho$). Substituting this expression then using orthogonality of L and R handed signals gives an expression for the SNR lost in terms of the intrinsic L and R handed amplitudes $\rho_{R,L}$ and the *overlaps* $(R, \hat{\psi}_R)$ and $(L, \hat{\psi}_L)$ between the two (normalized) line of sight R and L basis signals and our two R- and L-handed basis functions:

$$\frac{\rho_{rem}^2}{\rho^2} = 1 - \frac{1}{\rho_R^2 + \rho_L^2} [\rho_R^2 |(R, \hat{\psi}_R)|^2 + \rho_L^2 |(L, \hat{\psi}_L)|^2] \quad (30a)$$

In the above discussion we pessimistically perform a point-to-point comparison: we do not allow the R, L waveforms to vary in phase or time, neither relative to the signal ψ nor relative to one another. In practice, however, we want to mimic the response of a *template manifold*,

⁹ The traditional coordinate system for binary parameters adopts the *initial conditions* and *spin vectors*, rather than the geometry of the precessing binary as it passes through the sensitive band. Recent calculations suggest coordinates adapted to the center of the band and which phenomenologically encode precession will more transparently represent the available information; see, for example, Brown et al. [41].

¹⁰ Alternatively, one can estimate how much precession matters by comparing a precessing NR signal with a nonprecessing template family, including a full search over all possible component masses and emission directions. This challenge will be addressed in a subsequent publication, using existing and recently developed numerical and theoretical signal models.

including all physical signals that include our synthetic nonprecessing binary. Allowing for similar events at different times, a better diagnostic for lost signal power due to precession is

$$\frac{\rho_{rem,min}^2}{\rho^2} = \min_t \rho_{rem}^2(t) / \rho^2 \quad (30b)$$

where the minimum is over all candidate times t for the merger event specified by $|R\rangle, |L\rangle$.

This “missing power” diagnostic behaves qualitatively differently for nonprecessing and precessing binaries. For simplicity, consider a scenario dominated by just the leading-order $(l, m) = (2, \pm 2)$ emission dominates, so higher harmonics can be omitted to a first approximation, such as $M = 100M_\odot$ and the initial LIGO noise curve. For a nonprecessing binary and for masses dominated by quadrupole emission, the two overlaps $|(R, \hat{\psi}_R)|$ and $|(L, \hat{\psi}_L)|$ are nearly unity. Hence, almost no signal power is lost. By contrast, precession introduces distinctive phase modulations that cannot be produced by nonprecessing sources [40, 41]. Since precession occurs during merger, we expect loss of signal amplitude in direct proportion to the phase and amplitude modulations that precession introduced. In the language of the above diagnostic, we expect that for precessing binaries the two overlaps $|(R, \hat{\psi}_R)|$ and $|(L, \hat{\psi}_L)|$ are substantially less than unity.

As an example, Figure 10 shows contour plots of these two overlaps (top panel) and of the total signal amplitude lost (bottom two panels) for a fiducial precessing binary. In this figure, we adopt a *low* reference mass ($M = 100M_\odot$) to insure both that $l = 2$ emission dominates and occurs along a relatively stationary instantaneous direction; see, e.g., Figure 2 in [27]. Even in this limit, the bottom left panel of Figure 10 shows that most orientations are poorly fit with an optimal nonprecessing approximation generated from the corotating frame. Further, these poorly-fit orientations lie nearly perpendicular to some instantaneous \hat{V} direction. Finally, in each of these poorly-fit orientations, the *relative phase of L and R* changes significantly. As seen in the bottom right panel, while the phase of $\psi_{4R,L}$ *individually* resemble a nonprecessing waveform, *together* their relative phase evolves in a way we expect that no single nonprecessing system could reproduce. Similar behavior occurs for all the precessing binaries we have explored.

Though we adopt a particularly well-chosen reference signal, this calculation only concretely demonstrates a this particular precessing binary has many lines of sight where its signal cannot be fit by this particular pair of nonprecessing basis signals. Real nonprecessing searches compare each individual signal with a *template bank* of many candidate nonprecessing signals. We will address this “fitting factor” problem in a subsequent publication that compares our precessing signals to a family of nonprecessing sources. However, motivated by other studies of precession-induced modulations [41], we anticipate

that *any* nonprecessing signal cannot mimic sufficiently strong geometric precession-induced phase and amplitude modulations.

D. Estimating the mismatch

Motivated by low-mass results [41], our calculations suggest a familiar conclusion: when viewed near its instantaneous orbital plane, a precessing binary can produce complicated emission, delicately balancing left and right handed power. No nonprecessing signal model can reproduce it. Of course, our signal model also neglects higher harmonics. Some of the mismatch seen in Figure [?] reflects our inability to recover these other modes. For the mass region considered, however, the modes not included produce only a few percent of the (corotating-frame) signal power; see Table 1 in [27]. The lack of higher harmonics cannot explain the extremely low matches seen here.

Low-mass studies suggest precession introduces coherent phase and amplitude modulations, superimposed on top of secular (corotating-frame) evolution [41]. A sufficiently generic nonprecessing model can fit any *secular* phase, but not the modulations. To show this, we will rewrite the line-of-sight left- and right-handed signal $\hat{\psi}_{4R,L}(t)$ as a modulation factor times a corotating-frame signal. Doing so will let us calculate the overlap between corotating-frame modes and any line of sight as a simple integral, whose integrand has two factors: (a) *secular* terms, reflecting the corotating modes’ slow change in amplitude with time; and (b) a *geometrical, precession term* \mathcal{X} , reflecting the change in amplitude and phase along the line of sight. These expressions prove the signal power “lost” in comparing a nonprecessing to precessing model can be uniquely associated to the *modulations* that precession introduces in the signal model – modulations that no nonprecessing signal can reproduce. For brevity and for practical reasons – almost all search strategies use the $(2, \pm 2)$ modes alone – we emphasize a sufficiently low reference mass that the signal is dominated by the $(l, m) = (2, 2)$ and $(2, -2)$ modes in its corotating frame. As noted above, higher order harmonics $l > 2$ are still significant at these masses [Table 1 in [27]]. Nonetheless, we explicitly neglect contributions from $l > 2$, both to demonstrate our analytic control over the problem and to connect to nonprecessing searches.

The line-of-sight gravitational wave signal $\psi_4(\hat{n}, t)$ can be expressed in terms of corotating-frame harmonics ψ_{4lm}^{corot} and a rotation operation:

$$r\psi_4(\hat{n}, t) = \sum_{m,m'} D_{mm'}^2(R(t)) \psi_{4m'}^{corot} Y_{2m}^{(-2)}(\hat{n}) \quad (31)$$

where $R(t)$ is a suitable rotation (e.g., the forward transformation $\hat{z} \rightarrow \hat{V}(t)$) and $D_{mm'}^l$ is a Wigner D matrix describing the action of $SU(2)$ rotations on angular eigenstates. If the corotating-frame $(2, \pm 2)$ modes dominate,

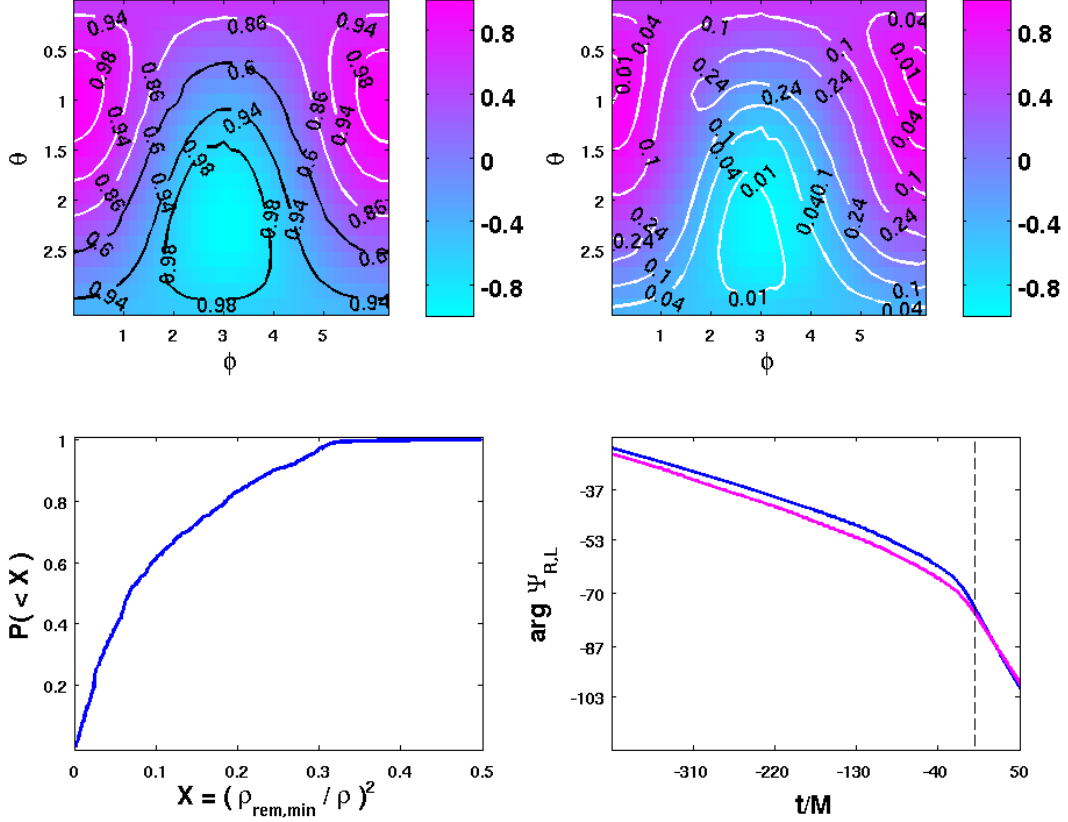


FIG. 10: **Nonprecessing approximation omits signal power:** Comparison of corotating $(2, \pm 2)$ subspace with the sum of all $l = 2$ modes along each line of sight, for the Sq(4,0.6,90,9) simulation and $M = 100M_\odot$. This binary preferentially emits L-handed signal into our detector's sensitive band [$\bar{\rho}_L/\bar{\rho}_R = 0.76$ from Table I]. *Top left panel:* Contours of normalized matches $|\langle R, \hat{\psi}_R \rangle|$ (white) and $|\langle L, \hat{\psi}_L \rangle|$ (black) for the Advanced LIGO noise curve at 100Mpc. For comparison, the colors indicate proximity to a single direction $(\hat{n}(\theta, \phi) \cdot \hat{V}^*)$ for $\hat{V}^* \equiv \hat{n}(1.01, 2.98)$, the estimated preferred emission direction at $100M_\odot$. The R basis signal is a good match when it dominates emission and vice-versa. *Top right panel:* Contour plot of $\rho_{rem,min}^2/\rho^2$, the fraction of signal power lost in a nonprecessing approximation [Eq. (30)]. [This calculation allows *independent timeshifts in L and R* and therefore underestimates the true fraction of power lost.] In directions nearly perpendicular to the preferred direction \hat{V}^* defined above, a nonprecessing approximation fails to capture all available signal information. *Bottom left panel:* Fraction $P(<X)$ of orientations with $\rho_{rem,min}^2/\rho^2$ less than a specific threshold (i.e., which lose less than a specified fraction of the signal amplitude with a natural nonprecessing approximation). A significant fraction of all orientations are significantly impacted by precession. *Bottom right panel:* For the line of sight $(\theta, \phi) = (0.94, 0.94)$, the phase of ψ_{4R} (magenta) and ψ_{4L} (blue) are shown. The two differ by a significant, time-varying phase ($\arg(z)$). While each polarization still resembles a nonprecessing signal, no single nonprecessing signal model can fit both R and L polarizations simultaneously. For this reason, along this line of sight a large fraction of the signal power is lost when fitting with a nonprecessing approximation (top right panel).

the line-of-sight signal can be approximated by just two terms:

$$r\psi_4^{est}(\hat{n}, t) \simeq \psi_{422}^{corot} \mathcal{X}_R + \psi_{42-2}^{corot} \mathcal{X}_L \quad (32)$$

$$\mathcal{X}_R \equiv \sum_m D_{m2}(R(t)) Y_{2m}^{(-2)}(\hat{n}) \quad (33)$$

$$\mathcal{X}_L \equiv \sum_m D_{m-2}(R(t)) Y_{2m}^{(-2)}(\hat{n}) \quad (34)$$

The two slowly-varying but not constant functions $\mathcal{X}_{R,L}$ depend only on *geometric* factors: our line of sight \hat{n} and

the rotation operator R (i.e., on \hat{V}).

The variation of $\mathcal{X}_{R,L}$ with time is completely responsible for the structure seen in Figure 10. In Sec. IV C, we described a nonprecessing-signal search strategy, where each line of sight was projected into the span of two corotating-frame basis signals $\propto \psi_{42\pm 2}^{corot}$. If the two modulation factors $\mathcal{X}_{R,L}$ were *constant*, these projections would be trivial; the search would recover the line-of-sight signal. To estimate the fraction of signal power lost due to precession, we further approximate the right- and

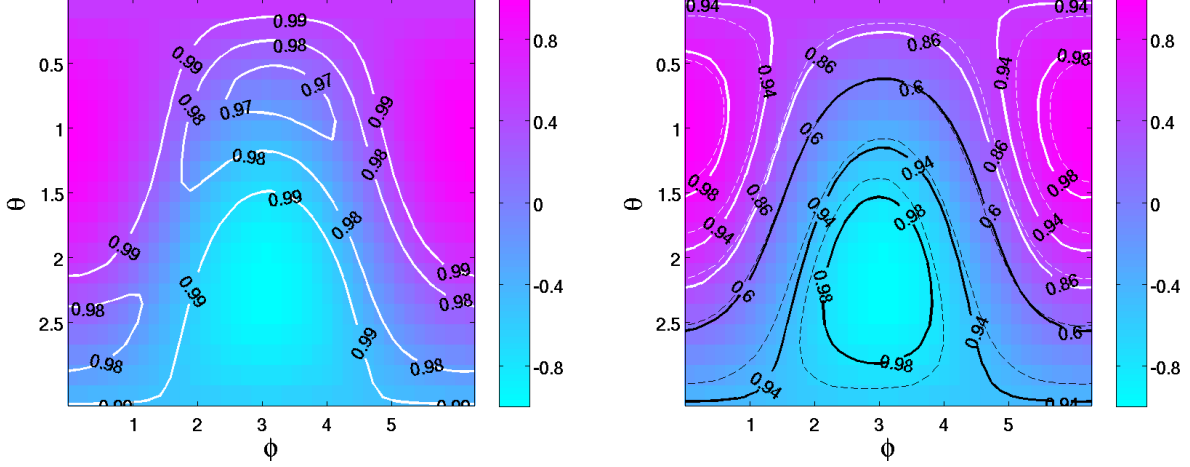


FIG. 11: **The line of sight estimate, Eq. 32, is a good approximation for the full $l = 2$ waveform:** Comparison of ψ_4^{est} with the sum of all $l = 2$ modes along each line of sight, for the Sq(4,0.6,90,9) simulation and $M = 100M_\odot$. As before, the colors indicate proximity to a single direction ($\hat{n}(\theta, \phi) \cdot \hat{V}^*$ for $\hat{V}^* \equiv \hat{n}(1.01, 2.98)$), the estimated preferred emission direction at $100M_\odot$. *Left panel:* Contour of the normalized match, $|(\psi_4^{est}, \psi_4)|$, for the Advanced LIGO noise curve at 100Mpc. *Right panel:* Contours of normalized matches $|(R, \hat{\psi}^{est})| = |(R, \hat{\psi}_R^{est})|$ (white) and $|(L, \hat{\psi}^{est})| = |(L, \hat{\psi}_L^{est})|$ (black) for the Advanced LIGO noise curve at 100Mpc. For comparison, the thin dashed lines are the same as those in Fig. 10's top left panel.

left-handed parts of $\psi_4^{est}(\hat{n}, t)$ [Eq. (4)] by

$$\psi_{4R}^{est} \simeq \psi_{422}^{corot} \mathcal{X}_R \quad (35)$$

$$\psi_{4L}^{est} \simeq \psi_{42-2}^{corot} \mathcal{X}_L \quad (36)$$

which is an excellent approximation to the extent that $\mathcal{X}_{R,L}$ are slowly-varying. Given this ansatz, the formulae described in Sec. IV C let us calculate the fraction of signal-to-noise ρ_{rem}/ρ that a nonprecessing search should miss when applied to this particular line of sight. For example, the overlap $\langle R, \hat{\psi}_R \rangle$ can be approximated by $\langle R, \hat{\psi}_R^{est} \rangle$, which can in turn be approximated as

$$\langle R, \hat{\psi}_R^{est} \rangle \simeq \frac{\langle R | \mathcal{X}_R | R \rangle}{\langle R | \mathcal{X}_R |^2 | R \rangle^{1/2}} \quad (37)$$

$$= \frac{\langle \hat{\psi}_R | \mathcal{X}_R^{-1,*} | \hat{\psi}_R \rangle}{\langle \hat{\psi}_R | \mathcal{X}_R |^{-2} | \hat{\psi}_R \rangle^{1/2}} \quad (38)$$

$$= \frac{\int_0^\infty df \frac{\mathcal{X}_R |\psi_{422}^{rot}|^2}{(2\pi f)^4 S_h}}{\sqrt{\int_0^\infty df \frac{|\mathcal{X}_R \psi_{422}^{rot}|^2}{(2\pi f)^4 S_h}}} \quad (39)$$

where we have simplified the integral limits using chirality. A similar expression applies to the other chirality:

$$\langle L, \hat{\psi}_L^{est} \rangle \simeq \frac{\langle L | \mathcal{X}_L | L \rangle}{\langle L | \mathcal{X}_L |^2 | L \rangle^{1/2}} \quad (40)$$

$$= \frac{\int_{-\infty}^0 df \frac{\mathcal{X}_L |\psi_{42-2}^{rot}|^2}{(2\pi f)^4 S_h}}{\sqrt{\int_{-\infty}^0 df \frac{|\mathcal{X}_L \psi_{42-2}^{rot}|^2}{(2\pi f)^4 S_h}}} \quad (41)$$

Combined these two approximations allow us to approximate Fig. 10. These approximations suggest that mis-

match results from fluctuations in \mathcal{X} around their median values. To be concrete, the total SNR lost due to applying a nonprecessing approximation can be expanded as

$$\begin{aligned} \rho_{rem}^2 &= \langle \psi_4 | [1 - |R\rangle \langle R| - |L\rangle \langle L|] | \psi_4 \rangle \\ &= \rho_R^2 \left[1 - \frac{|\langle R | \mathcal{X}_R | R \rangle|^2}{\langle R | \mathcal{X}_R |^2 | R \rangle} \right] + \rho_L^2 \left[1 - \frac{|\langle L | \mathcal{X}_L | L \rangle|^2}{\langle L | \mathcal{X}_L |^2 | L \rangle} \right] \end{aligned} \quad (42)$$

For a nonprecessing binary with a fixed preferred direction, the geometrical quantities \mathcal{X} remain constant. By contrast, for a precessing binary, \mathcal{X} fluctuates, with the fraction of lost power being proportional to rms fluctuations in \mathcal{X} .

Though simple, these expressions are surprisingly powerful. In particular, they allow us to estimate *the critical threshold for precession, above which its effect is observationally accessible, at a given mass and amplitude*. As a simple rule of thumb, a physical process or parameter can impact a Bayesian posterior if the match changes by of order $1/\rho^2$ for $\rho \simeq 10$ the signal amplitude. Using nonprecessing waveforms $\psi_{2\pm 2}$ and synthetic precession trajectories \hat{V} , we can efficiently explore what lines of sight and what precession trajectories permit an observationally significant amount of precession. We will return to this subject in a subsequent publication.

As in previous studies of precession [41], our analysis lends itself to geometric interpretation and approximation. For example, early in the inspiral, the orbital frequency is both well-defined and shorter than all other scales. A separation of timescales argument suggests that the time-domain multiplication $\mathcal{X}_R |R\rangle$ could be implemented as a *frequency-domain* multiplication

$\mathcal{X}_{R,L}(t(f))$. In this limit, the inner products $(R, \hat{\psi}_R)$ and $(L, \hat{\psi}_L)$ become (frequency) *averages* over the signal. This approach has been used to calculate fitting factors between nonprecessing searches and precessing black hole/neutron star binaries [41]. Further investigation is needed to determine whether a separation-of-timescales approximation remains useful during the merger and ringdown phase.

V. CONCLUSIONS

Our paper makes two claims: first, that significant “orientation” or “polarization” changes occur after the merger of two binary black holes; and, second, that these changes could be accessible even to present-day detectors, if a source could be detected.

First and foremost, in this paper we report on and provide a simple phenomenological interpretation of rapid changes in the gravitational wave emission of merging, precessing black hole binaries at and beyond merger. Phenomenologically, the features we report on correspond to coherent, multimodal oscillations in the merger and ringdown signal that resemble “precession” of the remnant black hole. We confirm their existence through two time-domain methods: first with “polarization”, the ratio of left- to right-handed emission; and second using a preferred direction that traces the direction of strongest emission. We provide a simple rule to explain the amplitude and phase of these oscillations in terms of coherent, long-lived “precession” of the black hole binary before and the merger remnant after merger. Our interpretation agrees with a recently-developed geometric interpretation for high-frequency Kerr quasinormal modes [28]. This correspondence merits further investigation.

Second, using data-analysis-motivated diagnostics, we demonstrate each line of sight carries information about its orientation relative to the preferred orientation described above. For the simulations we have performed, we are able to explicitly show that a nonprecessing search will perform poorly, in extreme but not uncommon cases losing $\simeq 20\%$ of signal power even at low mass ($M \simeq 100M_\odot$). For sufficiently loud signals, we furthermore suggest that the polarization can be measured *nonparametrically*. By analogy with low mass binaries, we expect that the most rapid phase evolution characterizes the binary component masses and spins, while secular modulations encode the orientation and spins. To summarize, the short signal from merging waveforms carries a surprising amount of information about merger dynamics. Our analysis suggests this information can be phenomenologically extracted, even without a complete and physically-parameterized model for the waveform.

Our study has significant implications for present data analysis and parameter estimation strategies. First and foremost, our proof-of-concept study shows how data analysis strategies can extract easily-understood physics from complicated, short, multimodal gravitational wave

signals. Second, our analysis suggests that nonprecessing models (phenomenological; ringdown; et cetera) for high-mass sources ($M > 100M_\odot$) can omit significant features and introduce uncontrolled biases when applied to “typical” merger events, as typical events can involve significant post-merger oscillations. For example, our studies suggest that typical moderate-spin mergers produce a coherent, multimodal ringdown signal, with significant polarization changes along a typical line of sight. As another example, by analogy to studies of inspiralling low mass binaries [41], nonprecessing searches will be particularly ineffective for certain lines of sight and spin configurations. We will address the selection bias of nonspinning searches for precessing binary mergers in a subsequent publication.

From our preliminary investigations, we believe the surprisingly rich and rapid behavior of merging, precessing binary black holes may encode nonlinear features of strong-field gravity. For example, our analysis suggests that rapid orientation changes occur at merger, encoding a precession frequency. We anticipate that the pre- to post-merger transition coherently seeds a variety of quasinormal modes, with surprisingly long-lived coherence in the time domain. We suggest the relationship between the pre- and post-merger amplitudes of these coherent post-merger oscillations will provide valuable information about the strong-field merger process. All of the features described above can be extracted from simulations and observations using the techniques described in this work. We therefore suspect that strong polarization changes are observationally accessible features of strong-field gravity during binary black hole merger.

Acknowledgments

The authors have benefitted from conversations with Evan Ochsner, Chad Hanna, Kip Cannon, Andrew Lundgren, and Pablo Laguna. The authors thank Huan Yang and Aaron Zimmerman for pointing out reference [28].

DS is supported by NSF awards PHY-0925345, PHY-0941417, PHY-0903973 and TG-PHY060013N. ROS is supported by NSF award PHY-0970074, the Bradley Program Fellowship, and the UWM Research Growth Initiative.

-
- [1] Abbott et al. (The LIGO Scientific Collaboration), Reports on Progress in Physics **72**, 076901 (2009), URL <http://stacks.iop.org/0034-4885/72/i=7/a=076901>.
 - [2] F. Acernese and et al, Journal of Instrumentation **7**, P03012 (2012), URL <http://stacks.iop.org/1748-0221/7/i=03/a=P03012>.
 - [3] M. Punturo et al, Classical and Quantum Gravity **27**, 194002 (2010).
 - [4] L. Lehner, Class.Quant.Grav. **18**, R25 (2001), gr-qc/0106072.
 - [5] J. Centrella, J. G. Baker, B. J. Kelly, and J. R. van Meter, Reviews of Modern Physics **82**, 3069 (2010).
 - [6] F. Herrmann, I. Hinder, D. M. Shoemaker, P. Laguna, and R. A. Matzner, Phys. Rev. **D76**, 084032 (2007).
 - [7] F. Herrmann, I. Hinder, D. Shoemaker, P. Laguna, and R. A. Matzner, Astrophys. J. **661**, 430 (2007).
 - [8] J. Healy et al., Phys. Rev. Lett. **102**, 041101 (2009).
 - [9] A. Buonanno, G. B. Cook, and F. Pretorius, Phys. Rev. D **75**, 124018 (2007), URL <http://xxx.lanl.gov/abs/gr-qc/0610122>.
 - [10] J. Abadie et al. (LIGO Scientific Collaboration , Virgo Collaboration), Phys. Rev. D **83**, 122005 (2011).
 - [11] R. Owen, J. Brink, Y. Chen, J. D. Kaplan, G. Lovelace, K. D. Matthews, D. A. Nichols, M. A. Scheel, F. Zhang, A. Zimmerman, et al., Physical Review Letters **106**, 151101 (2011).
 - [12] D. A. Nichols, R. Owen, F. Zhang, A. Zimmerman, J. Brink, Y. Chen, J. D. Kaplan, G. Lovelace, K. D. Matthews, M. A. Scheel, et al., Phys. Rev. D **84**, 124014 (2011).
 - [13] N. Christensen and R. Meyer, Phys. Rev. D **58**, 082001 (1998).
 - [14] J. Veitch and A. Vecchio, Phys. Rev. D **78**, 022001 (2008).
 - [15] C. Röver, R. Meyer, G. M. Guidi, A. Viceré, and N. Christensen, Classical and Quantum Gravity **24**, 607 (2007).
 - [16] C. Röver, R. Meyer, and N. Christensen, Phys. Rev. D **75**, 062004 (2007).
 - [17] M. V. van der Sluys, C. Röver, A. Stroeer, V. Raymond, I. Mandel, N. Christensen, V. Kalogera, R. Meyer, and A. Vecchio, ApJL **688**, L61 (2008).
 - [18] M. van der Sluys, V. Raymond, I. Mandel, C. Röver, N. Christensen, V. Kalogera, R. Meyer, and A. Vecchio, Classical and Quantum Gravity **25**, 184011 (2008).
 - [19] N. Cornish, L. Sampson, N. Yunes, and F. Pretorius, Phys. Rev. D **84**, 062003 (2011).
 - [20] T. G. F. Li, W. Del Pozzo, S. Vitale, C. Van Den Broeck, M. Agathos, J. Veitch, K. Grover, T. Sidery, R. Sturani, and A. Vecchio, ArXiv e-prints (2011).
 - [21] W. Del Pozzo, J. Veitch, and A. Vecchio, Phys. Rev. D **83**, 082002 (2011).
 - [22] L. Boyle, M. Kesden, and S. Nissanke, Physical Review Letters **100**, 151101 (2008), URL <http://xxx.lanl.gov/abs/arXiv:0709.0299>.
 - [23] Y. Zlochower, R. Gómez, S. Husa, L. Lehner, and J. Winicour, Phys. Rev. D **68**, 084014 (2003), arXiv:gr-qc/0306098.
 - [24] H. Nakano and K. Ioka, Phys. Rev. D **76**, 084007 (2007), 0708.0450.
 - [25] E. Pazos, D. Brizuela, J. M. Martín-García, and M. Tiglio, Phys. Rev. D **82**, 104028 (2010), 1009.4665.
 - [26] R. O’Shaughnessy, B. Vaishnav, J. Healy, Z. Meeks, and D. Shoemaker, Phys. Rev. D **84**, 124002 (2011), URL <http://link.aps.org/doi/10.1103/PhysRevD.84.124002>.
 - [27] R. O’Shaughnessy, J. Healy, L. London, Z. Meeks, and D. Shoemaker, Phys. Rev. D **85**, 084003 (2012), URL <http://xxx.lanl.gov/abs/1201.2113>.
 - [28] H. Yang, D. A. Nichols, F. Zhang, A. Zimmerman, Z. Zhang, and Y. Chen, ArXiv e-prints (2012), 1207.4253.
 - [29] I. Hinder, B. Vaishnav, F. Herrmann, D. Shoemaker, and P. Laguna, Phys. Rev. **D77**, 081502 (2008).
 - [30] I. Hinder, F. Herrmann, P. Laguna, and D. Shoemaker, **arxiv:0806.1037** (2008).
 - [31] J. Healy, J. Levin, and D. Shoemaker, Phys. Rev. Lett. **103**, 131101 (2009).
 - [32] J. Healy, P. Laguna, R. A. Matzner, and D. M. Shoemaker, Phys. Rev. **D81**, 081501 (2010).
 - [33] T. Bode, R. Haas, T. Bogdanovic, P. Laguna, and D. Shoemaker, Astrophys. J. **715**, 1117 (2010).
 - [34] E. Schnetter, S. H. Hawley, and I. Hawke, Class. Quant. Grav. **21**, 1465 (2004).
 - [35] cactus-web, cactus Computational Toolkit home page: <http://www.cactuscode.org>.
 - [36] S. Husa, I. Hinder, and C. Lechner, Computer Physics Communications **174**, 983 (2006).
 - [37] T. A. Apostolatos, C. Cutler, G. J. Sussman, and K. S. Thorne, Phys. Rev. D **49**, 6274 (1994).
 - [38] E. Ochsner and R. O’Shaughnessy, in LSC review (DCC P120043); to be submitted to PRD (2012).
 - [39] P. Schmidt, M. Hannam, S. Husa, and P. Ajith, Phys. Rev. D **84**, 024046 (2011), URL <http://xxx.lanl.gov/abs/arXiv:1012.2879>.
 - [40] M. Boyle, R. Owen, and H. P. Pfeiffer, Phys. Rev. D **84**, 124011 (2011).
 - [41] D. Brown, A. Lundgren, and R. O’Shaughnessy, Submitted to PRD (arXiv:1203.6060) (2012), URL <http://arxiv.org/abs/1203.6060>.
 - [42] C. O. Lousto, M. Campanelli, Y. Zlochower, and H. Nakano, Classical and Quantum Gravity **27**, 114006 (2010).
 - [43] R. O’Shaughnessy, B. Vaishnav, J. Healy, and D. Shoemaker, Phys. Rev. D **82**, 104006 (2010), (arXiv:1007.4213), URL <http://xxx.lanl.gov/abs/arXiv:1007.4213>.

- [44] E. Berti, V. Cardoso, and A. O. Starinets, *Classical and Quantum Gravity* **26**, 163001 (2009), 0905.2975.
- [45] L. London, R. O’Shaughnessy, J. Healy, and D. Shoemaker, in preparation (????).
- [46] E. Poisson and C. M. Will, *Phys. Rev. D* **52**, 848 (1995), arXiv:gr-qc/9502040.
- [47] M. Vallisneri, *Phys. Rev. D* **77**, 042001 (2008), arXiv:gr-qc/0703086.
- [48] C. Cutler and E. E. Flanagan, *Phys. Rev. D* **49**, 2658 (1994), gr-qc/9402014.
- [49] V. Raymond, M. V. van der Sluys, I. Mandel, V. Kalogera, C. Röver, and N. Christensen, *Classical and Quantum Gravity* **26**, 114007 (2009), 0812.4302.
- [50] B. Aylott, B. Farr, V. Kalogera, I. Mandel, V. Raymond, C. Rodriguez, M. van der Sluys, A. Vecchio, and J. Veitch, ArXiv e-prints (2011), 1106.2547.
- [51] S. Nissanke, J. Sievers, N. Dalal, and D. Holz, *Astrophys. J.* **739**, 99 (2011), 1105.3184.
- [52] R. N. Lang, S. A. Hughes, and N. J. Cornish, *Phys. Rev. D* **84**, 022002 (2011), 1101.3591.
- [53] S. Klimenko, S. Mohanty, M. Rakhmanov, and G. Mitselmakher, *Phys. Rev. D* **72**, 122002 (2005), URL <http://arxiv.org/abs/gr-qc/0508068>.
- [54] S. Klimenko, I. Yakushin, A. Mercer, and G. Mitselmakher, *Classical and Quantum Gravity* **25**, 114029 (2008).
- [55] L. London, R. O’Shaughnessy, J. Healy, and D. Shoemaker, in preparation (????).